AD-A141 197 DEFORMATION AND FRACTURE MAPS FOR POLYMER-FOAMS SOLID POLYMERS AND POLYME..(U) CONSTRUCTION ENGINEERING RESEARCH LAB (ARMY) CHAMPAIGN IL M F ASHBY ET AL. 1/1

UNCLASSIFIED APR 84 CERL-TM-M-344 F/G 11/9 NL

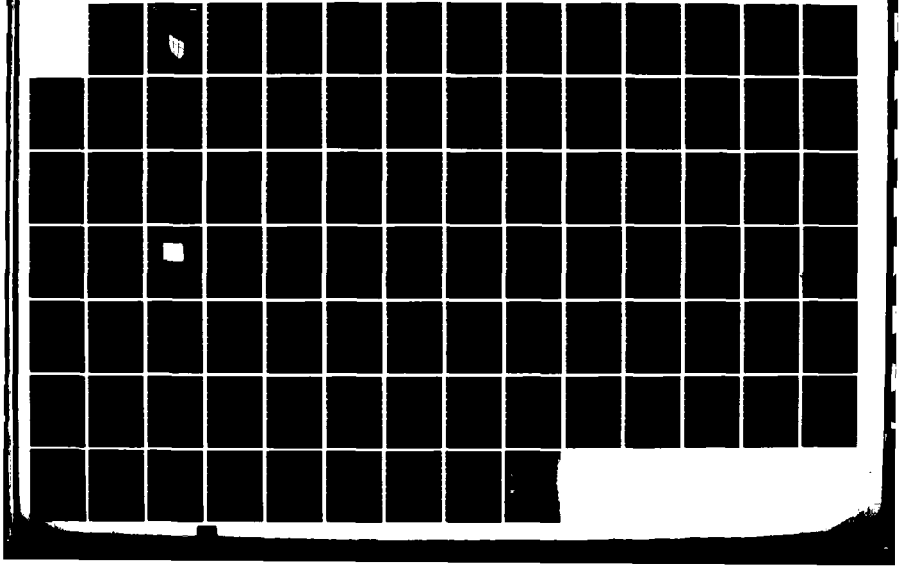

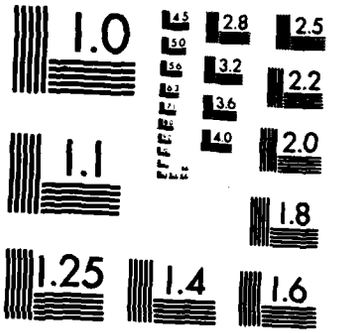

US Army Corps
of Engineers
Construction Engineering
Research Laboratory

TECHNICAL MANUSCRIPT M-344
April 1984

DEFORMATION AND FRACTURE MAPS FOR POLYMER-FOAMS, SOLID POLYMERS AND POLYMER-COMPOSITES

by
M. F. Ashby
P. W. R. Beaumont

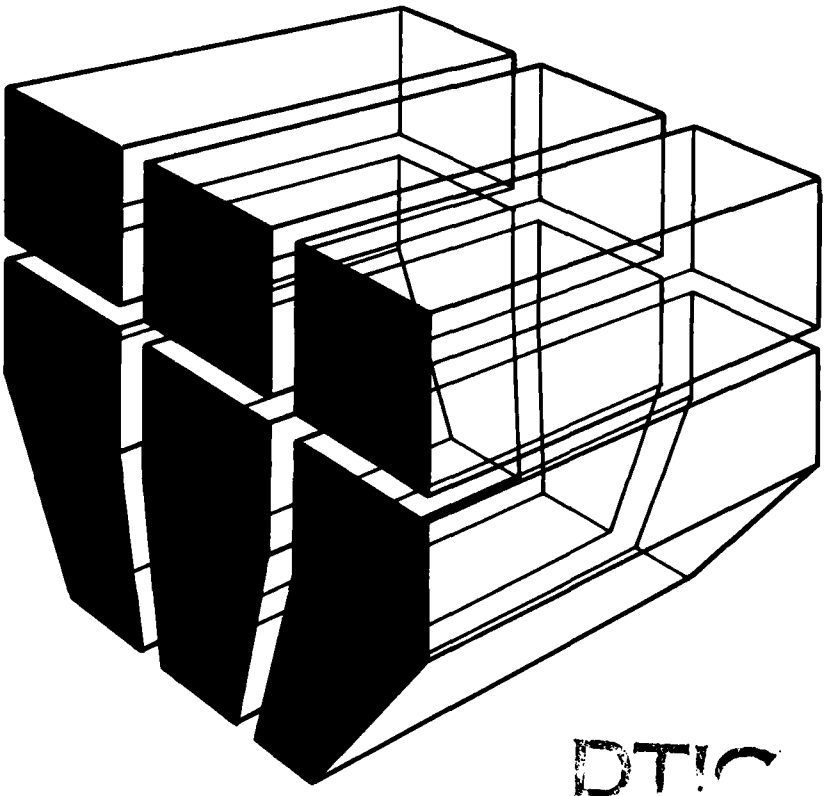

The contents of this report are not to be used for advertising, publication, or promotional purposes. Citation of trade names does not constitute an official indorsement or approval of the use of such commercial products. The findings of this report are not to be construed as an official Department of the Army position, unless so designated by other authorized documents.

DESTROY THIS REPORT WHEN IT IS NO LONGER NEEDED
DO NOT RETURN IT TO THE ORIGINATOR

UNCLASSIFIED

SECURITY CLASSIFICATION OF THIS PAGE (When Data Entered)

REPORT DOCUMENTATION PAGE		READ INSTRUCTIONS BEFORE COMPLETING FORM
1. REPORT NUMBER CERL-TM-M-344	2. GOVT ACCESSION NO. AD-A141 197	3. RECIPIENT'S CATALOG NUMBER
4. TITLE (and Subtitle) DEFORMATION AND FRACTURE MAPS FOR POLYMER-FOAMS, SOLID POLYMERS AND POLYMER-COMPOSITES		5. TYPE OF REPORT & PERIOD COVERED Final 6. PERFORMING ORG. REPORT NUMBER
7. AUTHOR(s) M. F. Ashby P.W.R. Beaumont		8. CONTRACT OR GRANT NUMBER(s) ARDSG-77-82
9. PERFORMING ORGANIZATION NAME AND ADDRESS Department of Engineering, University of Cambridge European Research Office, US Army London, ENGLAND		10. PROGRAM ELEMENT, PROJECT, TASK AREA & WORK UNIT NUMBERS 4A161102AT23-A-022
11. CONTROLLING OFFICE NAME AND ADDRESS U.S. ARMY CONSTRUCTION ENGINEERING RESEARCH LABORATORY P.O. Box 4005, CHAMPAIGN, IL 61820		12. REPORT DATE April 1984 13. NUMBER OF PAGES 77
14. MONITORING AGENCY NAME & ADDRESS(if different from Controlling Office)		15. SECURITY CLASS. (of this report) Unclassified 15a. DECLASSIFICATION/DOWNGRADING SCHEDULE

16. DISTRIBUTION STATEMENT (of this Report)

Approved for public release; distribution unlimited.

17. DISTRIBUTION STATEMENT (of the abstract entered in Block 20, if different from Report)

18. SUPPLEMENTARY NOTES

Copies are available from the National Technical Information Service
Springfield, VA 22161

19. KEY WORDS (Continue on reverse side if necessary and identify by block number)

polymers
foam
fracture (mechanics)
deformation

20. ABSTRACT (Continue on reverse side if necessary and identify by block number)

This report describes an initial study of the development of deformation and fracture maps for classifying polymeric-based materials. It is in three parts. Part I describes how the mechanical behaviour of polymer-foams can be classified in terms of the properties of the cell wall and cell geometry, where a diagram of applied stress and strain displays information of the mechanisms of deformation and buckling. Part 2 shows how solid

DD FORM 1 JAN 73 1473 EDITION OF 1 NOV 65 IS OBSOLETE

UNCLASSIFIED

SECURITY CLASSIFICATION OF THIS PAGE (When Data Entered)

BLOCK 20. (Cont'd).

polymers can be classified by their mechanical response and mechanisms of deformation based on diagrams of modulus versus temperature with contours of constant time. Finally, Part 3 shows how models of the mechanisms of fracture of advanced polymer-composites can be used to construct diagrams where any 2 of number of composite properties are plotted against one another and contours of constant toughness and certain failure parameters, together with the dominant fracture mechanisms, are displayed.

FOREWORD

This research was conducted by the Engineering Department, Cambridge University, under contract number ARDSG-27-82, from the European Research Office, London. The studies were sponsored by the U.S. Army Construction Engineering Research Laboratory (USA-CERL) for the Office of the Chief of Engineers (OCE). The work was conducted under Project 4A161102AT23, "Basic Research in Military Construction"; Task A, "Base/Facility Development"; and Work Unit 022, "Mechanical Properties of Polymers," of which it is one of several sub-tasks in the research. The overall research is designed to provide a better understanding of the micromechanics of deformation and rupture of polymer chains so that bulk material performance is better understood and acceptable design values for polymer-based materials can be provided to engineer and architect designers.

The USA-CERL Principal Investigator is Mr. Alvin Smith of the Engineering and Materials Division (EM). Dr. Robert Quattrone is Chief, USA-CERL-EM.

COL Paul J. Theuer is Commander and Director of CERL, and Dr. L. R. Shaffer is Technical Director.

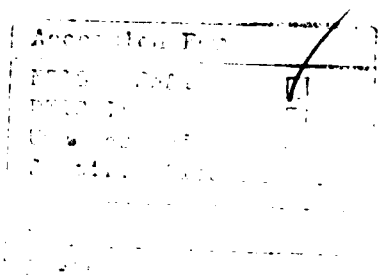

A-1

CONTENTS

		Page
	DD Form 1473	1
	FOREWORD	3
	LIST OF TABLES AND FIGURES	5
PART 1.	DEFORMATION-MODE MAPS FOR POLYMER-FOAMS	9
	Summary	9
	The Structure of Cellular Solids	9
	Deformation Mechanisms and Idealized Foam Structures	10
	Mechanical Properties	11
	Linear Elastic Properties	11
	Non-Linear Elastic Behavior	12
	Plastic Yielding	13
	Plastic Indentation	14
	The Crushing Strength	14
	The Tensile Fracture Stresses	15
	Overall Mechanical Response: Deformation Maps	17
	Deformation Map for Elastomeric Foams	17
	Plastic Foams	19
	Rigid Foams	20
	Selection of Foams for Mechanical Design	20
	Conclusions	21
	References	22
	Tables and Figures	24
PART 2.	DEFORMATION MAPS FOR SOLID POLYMERS	43
	Summary	43
	Introduction	43
	The Glassy Modulus	44
	The Glass-Rubber (or Viscous) Transition	46
	The Rubbery Modulus	49
	Newtonian-Viscous Flow	50
	Data for PMMA	50
	Construction of the Maps	51
	Conclusions	51
	References	52
	Figures	53
PART 3.	FRACTURE MAPS FOR POLYMER-COMPOSITES	56
	Summary	56
	Introduction	56
	Fracture Mechanisms	57
	Fracture Toughness Maps	58
	Debond Length and Pull-Out Length Equations	58
	Fibre Debonding and Fibre Pull-Out	58
	Prediction of Fibre Debond Length	59
	Prediction of Fibre Pull-Out Length	61
	Fracture Energy (Toughness) Equations	62
	Interfacial Surface Energy Equation	62
	Fibre Elastic Energy Equation	63
	Fibre Pull-Out Energy Equation	64

CONTENTS (Cont'd)

	Page
Construction of the Maps	64
Method of Construction	64
Comparison Between Maps	65
A Case Study	65
Conclusions	66
References	66
Tables and Figures	67

TABLES

Number		Page
	PART 1	
1	Symbols and Units	24
2	Properties of Cell-Wall Materials	25
3	The Equations for Stiffness and Strength of Foams	26
	PART 3	
1	Material Parameters Which Appear in the Models	67
2	Typical Values of Material Properties Used	68
3	Summary of Fracture Property Dependence on Constitutive Properties of the Composite	69

FIGURES

	PART 1	
1	The Three-Dimensional Structure of Open and Closed-Cell Foams, Idealized	27
2	The Typical Shape of the Stress-Strain Curve for a Foam	27
3	The Linear-Elastic Deformation of a Foam	28
4	The Relative Young's Modulus, E/E_s, Plotted Against Relative Density, ρ/ρ_s	29
5	The Non-Linear Deformation of a Foam	30
6	The Relative Elastic Collapse Stress, σ^*_{el}/E_s, Plotted Against Relative Density, ρ/ρ_s	31
7	The Yielding of a Plastic Foam	32
8	The Relative Plastic Collapse Stress, σ^*_{pl}/σ_y, Plotted Against Relative Density, ρ/ρ_s	33
9	The Crushing of a Brittle Foam	34
10	The Relative Crushing Strength, σ^*_f/σ_f, Plotted Against Relative Density, ρ/ρ_s, for Brittle Foams	35
11	Mode 1 Crack Propagation in a Brittle Foam	36

FIGURES (Cont'd)

Number		Page
12	The Normalized Fracture Toughness, $K_{IC}/\sigma_f\sqrt{\pi\ell}$, Plotted Against, ρ/ρ_s, for Crack Propagation in Brittle Foams	37
13	A Deformation-Mechanism Map for Elastomeric Foams, for Relative Densities from 0.02 to 1	38
14	The Progressive Collapse of Cork, an Elastomeric Foam	39
15	A Deformation-Mechanism Map for a Plastic Foam, for which $\sigma_y/E_s = 0.05$, for Relative Densities From 0.05 to 1	40
16	The Progressive Collapse of Cells in an Aluminum Honeycomb	41
17	A Deformation-Mechanism Map for a Rigid Plastic Foam, for Which $\sigma_y/E_s = 0.1$, for Relative Densities From 0.01 to 1	42
	PART 2	
1	Comparison of Experimental Curves and Master Stress Relaxation Curve for Polymethyl Methacrylate	53
2	Comparison of Master Stress Relaxation Curve, Calculated From the Distribution of Relaxation Times	53
3	Total Volume, V, and Occupied Volume, V_o, as a Function of Temperature	54
4	Standard Linear Solid Represented by a Model of Springs and Dashpot	54
5	A Deformation Map for the Glassy Polymer PMMA	55
	PART 3	
1	A Fracture Map for E-Glass/Epoxy	70
2	A Schematic of the Crack Tip Region in a Brittle, Unidirectional Fibrous Composite	71
3	Stress Distribution Along the Length of a Debonded Fibre	72
4	Stress Profile in a Debonded Fibre, Together with the Variation of Fibre Strength to Show the Location of a Fibre Break (Point A)	73
5	Schematic of Debonded and Pulled-Out Fibres and Bundles From a Cracked Matrix	74

FIGURES (Cont'd)

Number		Page
6	Stress Profiles in an Unbroken and Broken Fibre	75
7	A Fracture Map for HM Carbon/Epoxy	76
8	A Fracture Map for HS Carbon/Epoxy	77
9	A Fracture Map for Kevlar 49/Epoxy	78
10	A Fracture Map for E-Glass/Epoxy	79
11	A Fracture Map for (0/90) E-Glass Epoxy with Experimental Toughness Data Superimposed	87

PART I DEFORMATION-MODE MAPS FOR POLYMER-FOAMS

Summary

The mechanical properties (elastic, plastic, creep and fracture) of cellular solids or foams are related to the properties of the cell wall material and to the cell geometry. The properties are well described by simple formulae. Such materials occur widely in nature and have many potential engineering applications.

1. THE STRUCTURE OF CELLULAR SOLIDS

Making foams is not difficult. Most polymers can be foamed easily, and techniques exist for doing the same thing with ceramics and glasses. Even metals can be formed into foams.

Some foams are almost *isotropic*, meaning that their structure and their properties have no directionality. Others are *anisotropic*: their structure is axisymmetric (like cork) or orthotropic (like wood); and their properties reflect this. Man-made foams tend to be almost isotropic. Natural cellular solids are rarely so; a single piece of cork or bone differs in strength and stiffness by a factor of 2 or more along two directions at right angles.

There is a second distinction. Some foams have *closed cells* (like a soap foam): the solid material is distributed in little plates which form the faces of the cells. Others have *open cells* (like a sponge): the solid material is distributed in little columns or beams which form the cell edges. The mechanical properties reflect, to some extent, this distribution. In reality, most man-made foams, even those with closed cell faces, behave like open-celled foams because surface tension draws much of the solid material into the cell edges during manufacture.

The most important aspect of the structure is the *relative density*, ρ/ρ_s, where ρ is the density of the foam and ρ_s that of the solid of which the foam is made. The mechanical properties of foams depend, above all else, on the relative density. It can vary from 1 to as little as 0.01 . The familiar foamed plastics used for packaging have a relative density of around 0.05 .

2. DEFORMATION MECHANISMS AND IDEALISED FOAM STRUCTURES

Detailed studies[1-4] of model foams have identified four *deformation modes*: linear elasticity, non-linear elasticity, plastic collapse and various sorts of fracture. The studies used 2-dimensional hexagonal cells, like those in the diagrams shown later in this paper. A hexagonal network is a good starting point because the modes of deformation correspond to those of 3-dimensional foams, yet the geometry is simple enough that a complete analysis is practical. The understanding derived from the 2-dimensional models has provided the foundation for the analysis of the more complicated problem presented by real, 3-dimensional foams[4-10] given below.

In the analysis, the 3-dimensional structure of the foam must be included. It is idealised, without loss of physically important features, in the models shown in Fig.1. The open-cell foam is modelled as a cubic array of members of length ℓ and square section of side t. Adjoining cells are staggered so that members meet at mid-points. The relative density of the cell, ρ/ρ_s (where ρ_s is the density of the cell wall material) is then given by:

$$\frac{\rho}{\rho_s} \propto \left(\frac{t}{\ell}\right)^2 \tag{1}$$

and the second moment of the section of a member (which we need later) is given by:

$$I = \frac{t^4}{12} \tag{2}$$

A closed-cell foam is modelled similarly. The square struts are replaced by square plates of side ℓ and thickness t. Adjoining cells are again staggered. Then:

$$\frac{\rho}{\rho_s} \propto \frac{t}{\ell} \quad , \quad I = \frac{\ell t^3}{12} \tag{3}$$

As pointed out earlier, most foams behave more like the first model, because surface tension concentrates material into the cell edges during their manufacture. We will use it as the basis of the calculations given below, which treat isotropic foams. Refinements, results for the second model and the generalisations to non-isotropic foams are given elsewhere[2,10]. Symbols are defined in Table 1.

3. MECHANICAL PROPERTIES

When a foam is compressed, the stress-strain curve shows 3 regions (Fig.2). At low strains, the foam deforms in a *linear-elastic* way; there is then a plateau of *deformation at almost constant stress*; and finally there is a region of *densification* as the cell walls crush together. The extent of each region depends on relative density ρ/ρ_s. Elastic foams, plastic foams, and even brittle foams all have 3-part stress-strain curves like this, though the mechanism causing the plateau is different in each case.

The deformation of a regular, 2-dimensional foam like that sketched in Fig.3, can be analysed with precision. It is far more difficult to do the same analysis for a 3-dimensional foam, because the response is an average of that of cell walls of random orientation in space, and with a distribution of length ℓ and section t^2. It is better to use the dimensional argument given below, and then rely on experiment to determine a single, unknown, constant of proportionality. This method, which we have used to analyse many properties of foams, will become clearer as it is applied in the following sections.

3.1 *Linear Elastic Properties*

When a foam is loaded, the cells walls at first *bend*[2,3,7,9,10]. Fig.3 shows this bending for the 2-dimensional model; the same bending deformation occurs in 3-dimensional foams. A force F, applied as shown, causes the non-vertical beams to deflect by δ, which is calculated from simple beam theory as:

$$\delta = \frac{C_1 F \ell^3}{12 E_s I} \tag{4}$$

Here C_1 is a resolution factor which depends only on the cell geometry and E_s is the Young's modulus of the solid cell wall material. For open cell foam of Fig.1(a) the stress is proportional to F/ℓ^2, the strain to δ/ℓ. The second moment of area, I, is proportional to t^4 (eqn. 2) giving:

$$E \propto E_s \frac{t^4}{\ell^4}$$

Using eqn.(1) for the density, we find:

$$\boxed{\frac{E}{E_s} = C_2 \left(\frac{\rho}{\rho_s}\right)^2} \tag{5}$$

where C_2 is a constant. The shear modulus scales in a similar way,

because shear deformation in a foam also causes simple bending of the cell walls[2].

Data are compared with eqn.(5) in Fig.4. It shows Young's moduli for polymeric and ceramic foams plotted against ρ/ρ_s on logarithmic scales. The full line is a plot of eqn.(5) with $C_2 = 1$; it gives a good description of a wide range of materials and densities. Note that the modulus falls rapidly as the volume of void space in the foam increases. The *range* of moduli practically available by foaming is large: it spans a factor of 10^4 . The modulus is important in the design of load-bearing structures which incorporate foams (sandwich panels for example).

3.2 *Non-Linear Elastic Behaviour*

Linear elasticity, of course, is limited to small strains, typically 5% in compression, rather more in tension. Elastomeric foams can be compressed far beyond this point. The deformation is still recoverable (and thus elastic) but is non-linear; it is caused by the *elastic buckling* of the columns or plates which make up the cell edges or walls[2,5,6,10] as shown in Fig.5, giving the plateau of the stress-strain curve* (Fig.2). It is exploited in cushions and packaging to give a restoring force (which we now calculate) which is independent of displacement.

The critical load at which a column of length ℓ , Young's modulus E_s and second moment of area I buckles is given by Euler's formula:

$$F_{cr} = \frac{n^2 \pi^2 E_s I}{\ell^2} \qquad (6)$$

The constant n^2 describes the degree of constraint at the ends of the column. If this load is reached for a layer of cells spanning the section, they will buckle, initiating the *elastic collapse* of the foam. For the 3-dimensional open-cell foam of Fig.1, the stress σ^*_{el} at which this occurs is proportional to F_{cr}/ℓ^2 , so that:

$$\sigma^*_{el} = n^2 \pi^2 \frac{E_s I}{\ell^4}$$

Using eqns.(1) and (2) we obtain:

*Several authors[3,9,14,19,20] studying the collapse of rigid foams sought to interpret their results as elastic buckling. Their calculations are in the spirit of that given here, but are inappropriate to the materials they studied.

$$\boxed{\frac{\sigma^*_{el}}{E_s} = C_3 \left(\frac{\rho}{\rho_s}\right)^2} \qquad (7)$$

valid for relative densities below 0.3 because, at higher densities, the cell walls are too short and stocky to buckle.

Data for σ^*_{el} for elastomeric foams are compared with eqn.(7) in Fig.6. They are well fitted by the equation with $C_3 = 0.05$. Like the modulus, the elastic collapse stress spans a wide range: for a given material, a range of 10^4 is accessible. This is important for the design of cushions, padding and packaging.

3.3 *Plastic Yielding*

Cellular materials can collapse by other mechanisms. If the cell-wall material is *plastic* (as are metals and many polymers) then the foam as a whole shows plastic behaviour. It is exploited in crash barriers and energy absorbing systems.

Plastic collapse occurs when the moment exerted on the cell walls by the force F exceeds the fully plastic moment, creating plastic hinges[2,10,21,22] as shown in Fig.7. For a beam of square section of side t, the fully plastic moment is:

$$M_p = \frac{1}{4} \sigma_y t^3 \qquad (8)$$

If a force F acts with a component normal to a beam of length ℓ, the maximum bending moment is proportional to $F\ell$. The stress on the foam, as before, is proportional to F/ℓ^2. Combining these results we find the plastic collapse stress of the foam to be:

$$\sigma^*_{pl} \propto \frac{M_p}{\ell^3}$$

Using eqn.(1) we obtain:

$$\boxed{\frac{\sigma^*_{pl}}{\sigma_y} = C_4 \left(\frac{\rho}{\rho_s}\right)^{\frac{3}{2}}} \qquad (9)$$

Data for the plastic deformation and for the plastic indentation of foams (discussed next) are plotted in Fig.8. They are well fitted by eqn.(9) with $C_4 = 0.3$ for relative densities of less than $\frac{1}{3}$ (at higher densities the cell edges are too short and stocky to bend plastically). The plastic collapse stress can be "tailored", by choosing a foam of the right density, over a range of 10^3. It is of primary importance in the design of crash padding and energy-absorbing foams.

3.4 *Plastic Indentation*

Unlike dense solids, which are incompressible when deformed plastically to large strains, foams change their volume when compressed. The cells of the foam collapse as the foam is squeezed, so that axial compression produces almost no lateral spreading. (Poisson's ratio for the plastic compression of low density foam is, typically, 0.04 [1,10,24,25]. Such foams yield plastically under a multiaxial state of stress when the maximum principal stress, not the octahedral shear stress, reaches the critical value σ^*_{pl} calculated in the last section.

Because of this, the indentation hardness of a foam is lower than that of a dense solid of the same yield stress: elements of the foam, compressed beneath the indenter, do not expand, and so are not constrained by the surrounding material in the same way that elements in a dense solid are. An analysis of the problem[16] shows that, for relative densities less than about 0.3, the intentation pressure, or "hardness" H of the foam is simply:

$$H = \sigma^*_{pl} \tag{10}$$

(instead of the result $H = 3\sigma_y$ for a dense solid). Two experimental studies[16,24] confirm this result. The data from the second study are included in Fig.8.

3.5 *The Crushing Strength*

Brittle foams (ceramics, and certain rigid polymers) collapse by yet other mechanisms: brittle crushing in compression[26], brittle fracture in tension[27,28]. The low crushing strength of refractory brick (a cellular solid) limits the loads than can be applied to it; and the low fracture toughness of foam can cause problems when they carry tensile loads, as they do in [illegible] panels.

Let the modulus of rupture* of the cell-wall material be σ_f. A cell wall will then fail (Fig.9) when the moment acting on it exceeds:

$$M_f = \frac{1}{6}\sigma_f t^3 \tag{11}$$

*The modulus of rupture of an elastic beam, loaded in bending, is the maximum surface stress in the beam at the instant of failure. The maximum stress is related to the moment by eqn.(11). The modulus of rupture for a brittle solid is often close to the tensile fracture strength.

As before, a force F, acting with a component normal to the wall of length ℓ, exerts a moment which is proportional to $F\ell$. The stress on the foam, as before, is proportional to F/ℓ^2. Combining these results we find that collapse by crushing will occur at the stress:

$$\sigma_f^* \propto \frac{M}{\ell^3} \propto \sigma_f \left(\frac{t}{\ell}\right)^3$$

Using eqn.(1), we obtain:

$$\boxed{\frac{\sigma_f^*}{\sigma_f} = C_7 \left(\frac{\rho}{\rho_s}\right)^{\frac{3}{2}}} \qquad (12)$$

There are few experimental measurements of the crushing of brittle foams. The limited data[18,22], shown in Fig.10, are insufficient to give confidence that eqn.(12) is a good description. But certain other observations do suggest that the model has the correct physical ingredients. First (and remarkably) the tensile and compressive fracture stress of unnotched foams should, according to the model, be equal (for brittle *solids*, the crushing strength is roughly 10 times the tensile strength). Measurements on foamed[18] glasses show that this is so. And, second, an extension of the model to describe crack propagation, and to predict the fracture toughness of foams, describes data well.

3.6 *The Tensile Fracture Stresses*

Compressive fracture is insensitive to defects - such things as flaws, cracks, or a few exceptionally large cells. But this is not so for tensile fracture. A completely unflawed sample, it is true, should sustain a tensile stress as high as that given by eqn. (12) before failing. But if it contained a crack or flaw, then the stress concentration it induces will fracture cell walls locally, extending the flaw and leading to sudden fracture (Fig. 11).

When a brittle foam is loaded, the cell walls at first deform elastically. The load is transmitted through the foam as a set of discrete forces and moments acting on cell walls. But, since the foam is *linear* elastic until the cell walls buckle, the average force and moment on a given cell wall can be calculated from the stress field in the equivalent linear-elastic continuum. We solve the discrete problem by taking the solution of the equivalent continuum problem (just as we do on a smaller scale in replacing the discrete bonds between atoms by a continuum) and using it to calculate the forces and moments on the discrete cell walls.

A crack of length a in an elastic solid, lying normal to a remote tensile stress σ^∞, creates a singular stress field:

$$\sigma = \frac{\sigma^\infty \sqrt{\pi a}}{\sqrt{2\pi r}} \tag{13}$$

at a distance r from its tip. Consider the first unbroked cell wall, which we take to be $\ell/2$ beyond the tip; it is subjected to a force:

$$F \propto \sigma \ell^2$$

where

$$\sigma = \sigma^\infty \sqrt{a/\ell}$$

This exerts a bending moment on the walls marked A and C, and bending moment plus a tensile stress on the wall marked B (Fig. 11). If, as before, the walls fail when the moment, proportional to F, exceeds the fracture moment given by eqn. (11), then the crack advances. Assembling these results gives:

$$\sigma^\infty \propto \frac{t^3}{\ell^3} \frac{\sigma_f}{\sqrt{a/\ell}}$$

where σ_f, as before, is the modulus of rupture of the cell wall. Using eqn. (1) we obtain:

$$\sigma^\infty = C_8 \left(\frac{\rho}{\rho_s}\right)^{\frac{1}{3}} \frac{\sigma_f}{\sqrt{a/\ell}} \tag{14}$$

where σ^∞ is the remote stress which will cause the crack to propagate. The equation is valid only when $a > \ell$ (otherwise there is no crack).

The result is just what would be expected. The fracture strength equals that for the unnotched material (eqn. 12) if the crack size is equal to the cell size. In an open-cell foam, a wall is either broken, or it is not. If the crack size is less than the cell size, no cell walls are broken and the foam is undamaged. Comparing eqn. (14) with the definition of K_{IC} (the plane-strain toughness) for a through-crack in an infinite sheet:

$$K_{IC} = \sigma^\infty \sqrt{\pi a}$$

we find

$$\boxed{\frac{K_{IC}}{\sigma_f \sqrt{\pi \ell}} = C_8 \left(\frac{\rho}{\rho_s}\right)^{\frac{3}{2}}} \tag{15}$$

Data for crack propagation in a brittle polymeric foam are plotted in Fig. 12. Eqn. (15), with $C_\beta = 0.65$, gives a good description of the data. Unlike all the other properties, K_{IC} depends on cell size. This, too, is expected: K_{IC} contains a dimension of length; the only lengths which enter the problem are the cell size ℓ and the wall thickness t, but that is related to ℓ through the relative density ρ/ρ_s (eqn. 1). The result is important whatever foams are used in load-bearing applications in which tensile forces appear - as they do in sandwich panels.

4. OVERALL MECHANICAL RESPONSE: DEFORMATION MAPS

When an elastomeric foam is compressed, it first deforms in a linear-elastic way; then its cells buckle to give non-linear elasticity; and, finally, the cells collpase completely and the stress rises rapidly as opposing cell walls are forced together. A plastic foam behaves in a somewhat similar way, except that, now, linear elasticity is followed by plastic collapse, and, finally, the forcing together of the cell walls. With brittle foams, progressive crushing can again lead to a plateau, ending when the material is completely crushed. The relevant formuli for open cell foams are summarised in Table 3, together with the equivalent results for true closed-cell foams (Fig.1b). Most man-made foams behave mechanically as if they had open cells, because surface tension (or other factors) concentrates the solid into the cell edges.

The extent of each phase of deformation depends on the relative density. It is convenient to display this behaviour as a *map* with axes compressive stress and compressive strain, showing the *fields* in which each mechanism is dominant. Superimposed on the field are *contours of constant (initial) relative density*.

4.1 *Deformation Map for Elastomeric Foams*

Fig. 13 shows a map for elastomeric foams. The linear elastic regime terminates when elastic buckling starts. The boundary of this

field (heavy solid line) lies at the strain at which elastic collapse starts. Froms eqns.(5) and (7), this strain is:

$$\varepsilon = C_3 = 0.05 \tag{16}$$

At relative densities above 0.3 the cell walls become so stocky that they can no longer buckle elastically. The curvature of the field boundary is such as to make the linear-elastic loading line for $\rho/\rho_s = 0.3$ tangent to the boundary.

The field of elastic buckling ends at the strain at which the foam finally "bottoms out", or densifies, with a rapid increase of load with displacement. This starts when the folding of the cells is so great that the walls begin to touch. We find that this begins when the foam has been compressed to a new relative density of about 0.5 (that is, the void space occupies half the volume), and it is complete when the foam has been compressed to a new relative density of 1 (no void space left).

During elastic buckling the foam compresses axially with no lateral spreading ($\nu = 0$). Then the relative density after a nominal compressure strain* ε is just $(\rho/\rho_s)(1/(1-\varepsilon))$. Equating this to 0.5 gives the strain at which densification starts:

$$\varepsilon_s = 1 - 2\frac{\rho}{\rho_s} \tag{17}$$

and equating it to 1 gives the strain at which densification is complete:

$$\varepsilon_c = 1 - \frac{\rho}{\rho_s} \tag{18}$$

(where ρ/ρ_s , of course, is the *initial* relative density). Within the elastic buckling field, the stress is related to the density by eqn.(7); using eqn.(17) gives the equation of the field boundary (heavy solid line) for the start of densification:

$$\varepsilon_s = 1 - 10\left(\frac{\sigma}{E_s}\right)^{\frac{1}{2}} \tag{19}$$

*Nominal compressive strain $\varepsilon = (h_o - h)/h_o$ where h_o is the original height and h the height after a compressive strain of ε .

The contours are stress-strain curves for foams of relative density vetween 10^{-2} and 1 . They show a linear elastic regime (eqn.5), and a plateau corresponding to elastic buckling (eqn.7); they start to bend upwards when densification starts (eqn.19) and approach a limiting slope of E_s when densification is complete (eqn.18). Within the field of elastic buckling the material can exist in two states at almost the same stress (rather like the p - v response of an ideal gas). It collapses in bands which broaden as strain increases: Fig.14, of cork, illustrates this.

The figure describes the overall response of all isotropic foams in compression. Elastomeric foams in tension show roughly linear-elastic response to rupture.

4.2 *Plastic Foams*

Plastic foams (Fig.15), like the elastic ones, show three regions: linear elasticity, plastic collapse, and densification - though now the strain beyond the linear-elastic regime is not recoverable.

The boundary of the linear-elastic field (heavy line) is obtained from eqns.(5) and (9); its equation is:

$$\frac{\sigma}{E_s} = (0.3 \frac{\sigma_y}{E_s})^4 \frac{1}{\epsilon^3} \qquad (20)$$

In constructing this map we have taken σ_y/E_s to be 0.05 . Next to the linear-elastic field is the field of plastic collapse. As before, two states of strain coexist at almost the same stress, so that complete collapse of part of the structure can occur while the rest is still elastic (Fig. 16); the bands of dense material broaden with increasing strain. Densification starts (as before) when the cell walls touch (eqn.17) and is complete when the relative density reaches 1 (eqn.19). The field boundary (heavy line) defining the start of densification is given, by the arguments leading to eqn.(19), by:

$$\epsilon = 1 - 4.5 \, (\frac{\sigma}{E_s} / \frac{\sigma_y}{E_s})^{\frac{3}{2}} \qquad (21)$$

Superimposed on the fields are stress-strain curves for foams of initial relative density between 0.05 and 1 . They show a linear elastic regime (eqn.5) and a plateau corresponding to plastic collapse (eqn.9); they start to bend upward when densification starts (eqn.21) and reach a limiting slope of E_s when densification is complete (eqn.18).

The figure shows the overall response of isotropic, plastic foams in compression. It is less general than the map for elastomeric foams because it must be constructed for a particular value of σ_y/E_s. But the equations show that the boundaries are not very sensitive to its value, and, for a given material, the diagram shows the behaviour for all densities.

4.3 *Rigid Foams*

Rigid foams show linear-elastic behaviour (eqn.5) to fracture. In compression, the foam crushes at constant stress (eqn.12), and since the crushing equation has the same form as that for plastic collapse, the behaviour will resemble that of Fig. 17. If the foam is contained, it will densify at the strain given approximately by eqn.(21), with σ_y/E_s replaced by σ_f/E_s.

4.4 *Selection of Foams for Mechanical Design*

The deformation-mode maps combine the data for a class of cellular solid with the understanding of the mechanisms of deformation. Flexible, or elastomeric foams, are widely used for cushions, padding and packaging. In these applications, it is the plateau stress, σ^*_{el} (eqn.7) and the extent of the plateau (given by inverting eqn.20) which are important. All this information is summarised, for all flexible foams, in a single map (Fig.13). It shows how, by judicious choice of E_s, ρ_s, and ρ/ρ_s, a foam best suited to the application can be chosen. Plastic or "rigid" foams are used for crash barriers and energy absorbing systems: the aim is to absorb energy while preventing the local stresses or loads from rising above the level which will injure or damage the contents of the package. For this purpose, a long plateau at a level σ^*_{pl} (eqn.9) below the damage level, is required. Again the necessary information is summarised in the diagram (Fig.15) which helps in the rational choice of foam material and density. The crushing of brittle foams is more of a problem than a property to be desired. The low crushing strength of refractory bricks limits the load which they can carry; and the crushing of bone is a problem when large compressive loads are applied to it. The deformation-mode map for a class of brittle cellular solids is identical to that for plastic foams (Fig.15) with σ_y/E_s replaced by σ_f/E_s, though the natural variability of brittle solids means that the predictive precision is lower.

There is considerable scope for developing the diagrams further, and for investigating diagrams to describe energy absorption by foams.

5. CONCLUSIONS

(a) When a cellular solid with a relative density below 0.30 is compressed, it shows a stress-strain curve with three parts: a linear-elastic part, a long plateau, and a regime of final densification. The properties of an entire class of such solids can be summarised as a deformation mode map, which shows how each of the three parts changes as the relative density changes. The method can be applied to natural materials, such as woods, to give a diagram which summarises the properties of that class of material.

(b) The mechanical properties of cellular solids can be modelled with precision. The models lead to constitutive laws (stress-strain relations) which have been thoroughly tested in simple compression. The response to multiaxial loading can be inferred, and the limited data are consistent with the inferences.

(c) The constitutive laws establish a basis for mechanical design with foams. The deformation-mode maps give a compact summary of properties, and give guidance in selecting foams for a specific application.

REFERENCES

1. Gibson, L.J. (1981) Ph.D. Thesis, Engineering Department, Cambridge University.

2. Gibson, L.J., Ashby, M.F., Schajer, G.S. and Robertson, C.I. (1982) Proc. R. Soc. Lond. A382, 25.

3. Patel, M.R. and Finnie, I. (1970) J. Materials 5, 909.

4. Abd. El Sayed, F.K., Jones, R. and Burgess, I.W. (1979) Composites 10, 209.

5. Gent, A.N. and Thomas, A.G. (1959) J. Appl. Polymer Sci. 1, 107.

6. Gent, A.M. and Thomas, A.G. (1963) Rubber Chem. Technol. 36, 597.

7. Ko, W.L. (1965) J. Cell. Plastics 1, 45.

8. Lederman, J.M. (1971) J. Appl. Polymer Sci. 15, 693.

9. Manges, G. and Knipschild, F. (1975) Polymer Eng. Sci. 15, 623.

10. Gibson, L.J. and Ashby, M.F. (1982) Proc. R. Soc. Lond. A382, 43.

11. Baxter, S. and Jones, T.T. (1972) Plastics Polymers 40, 69.

12. Phillips, P.J. and Waterman, N.R. (1974) Polymer Engng. Sci. 4, 67.

13. Moore, D.R. (1980) "The use of glass in engineering", Design Council Guide 05, Oxford: Univ. Press, 1975.

14. Chan, R. and Nakamura, M. (1969) J. Cell. Plastics 5, 112.

15. Brighton, C.A. and Meazey, A.E. (1973) Expanded polyvinyl chloride. In "Expanded Plastics - Trends in Performance Requirements" - A Micro Symposium organized by Q.M.C. Industrial Research Ltd., September 25, 1973, London.

16. Wilsea, M., Johnson, K.L. and Ashby, M.F. (1975) Int. J. Mech. Sci. 17, 457.

17. Walsh, J.B., Brace, W.F. and England, A.W. (1965) J. Am. Ceram. Soc. 48, 605.

18. Pittsburgh-Corning Inc. (1982) Foamglass Data Sheets.

19. Matonis, V.A. (1964) S.P.E. J1, Sept. 1024.

20. Barma, P., Rhodes, M.B. and Salovey, R. (1978) J. Appl. Phys. 49, 4985.

21. Thornton, P.H. and Magee, C.L. (1975) Met. Trans. 6A, 1253.

22. Thornton, P.H. and Magee, C.L. (1975) Met. Trans. 6A, 1801.

23. Traeger, R.K. (1967) J. Cell. Plastics 3, 405.

24. Shaw, M.C. and Sata, T. (1966) Int. J. Mech. Sci. 8, 469.

25. Rinde, J.A. (1970) J. Appl. Poly. Sci. 14, 1913.

26. Rusch, K.C. (1970) J. Appl. Poly. Sci. 14, 1263.

27. McIntyre, A. and Anderton, G.E. (1979) Polymer 20, 247.

28. Fowlkes, C.W. (1974) Int. J. Fracture 10, 99.

29. Roff, W.F. and Scott, J.R. (1971) "Fibres, Films, Plastics and Rubbers - A Handbook of Common Polymers". Butterworths, London.

30. Harper, C.A. (1975) "Handbook of Plastics and Elastomers". New York: McGraw-Hill.

31. Lazan, B.J. (1968) "Damping of Materials and Members in Structural Mechanics". Oxford: Pergamon Press.

32. Billmeyer, F.W. (1971) "Textbook of Polymer Science" (2nd Edn.). New York: Wiley Interscience.

33. Bonnin, M.J., Dunn, C.M.R. and Turner, S. (1969) Plastics Polymers 37, 517.

34. Oliver, D.S. (1980) "The Use of Glass in Engineering", Design Council Guide 05. Oxford: Univ. Press, 1975.

35. Easterling, K.E., Harrysson, R., Gibson, L.J. and Ashby, M.F. (1982) Proc. R. Soc. Lond. A383, 31.

36. Gibson, L.J. (1983) to be published.

TABLE 1: SYMBOLS AND UNITS

ρ	Density of foam (kg/m^3)
ρ_s	Density of cell-wall material (kg/m^3)
E	Young's Modulus of foam (MPa)
E_s	Young's Modulus of cell-wall material (MPa)
σ^*_{el}	Elastic collapse stress of elastomeric foam (MPa)
σ^*_{pl}	Plastic collapse stress of plastic foam (MPa)
σ_y	Yield strength of cell-wall material (MPa)
$\dot{\varepsilon}$	Strain rate (s^{-1})
$\dot{\varepsilon}_o, \sigma_o, n$	Creep constants (s^{-1}, MPa, -)
σ^*_f	Crushing strength of brittle foam (MPa)
σ_f	Modulus of rupture of cell-wall material (MPa)
K_{IC}	Fracture toughness of foam (MPa $m^{\frac{1}{2}}$)
t	Cell wall thickness (m)
ℓ	Cell size or cell wall length (m)
a	Half-length of crack (m)
I	Second moment of area of cell wall (m^4)
F	Force acting on a cell wall (N)
F_{cr}	Euler buckling load for cell wall (N)
M_p	Fully plastic moment of cell wall (Nm)
M_f	Moment which will just fracture cell wall (Nm)
$C_1 - C_8$	Dimensionless constants
$B_1 - B_8$	Dimensionless constants

TABLE 2: PROPERTIES OF CELL-WALL MATERIALS

REFERENCE	MATERIAL	ρ_s (Kg m^{-2}	E_s (MPa)	σ_y (MPa)	σ_f (MPa)
Baxter & Jones[11]	expanded polystyrene	1020[11]	2650[11]	---	
Brighton & Meazey[15]	expanded polyvinyl chloride	1400[29,30]	3000[29,30]	49[29,30]	
Chan & Nakamura[14]	extruded polystyrene	1050[14]	1400[14]	---	
Gent & Thomas[5]	rubber latex foam	----	2.64[5]	---	
Gibson & Ashby[10]	open-cell flexible polyurethane	1200[29]	45[31]	---	
Gibson & Ashby[10]	closed-cell flexible cross-linked polyethylene	910[32]	200[32]	---	
Gibson & Ashby[10]	closed-cell rigid polyurethane	1200[29]	1600[3]	127[31]	
Lederman[8]	rubber latex foam	----	----	---	
Matonis[19]	rigid polystyrene	1050[29]	1380[19]	79[19]	
Moore et al.[13]	polypropylene copolymer	902[33]	1130[33]	---	
	polystyrene acrylonitrile	1065[13]	3670[13]	---	
Patel & Finnie[3]	rigid polyester-based polyurethane	1230[3]	1600[3]	127[3]	
Phillips & Waterman[12]	rigid polyurethane	1200[29]	1600[3]	---	
Traeger[23]	rigid polyurethane foam	1200[29]	1600[3]	127[3]	
Wilsea et al.[16]	rigid polyurethane	1200[29]	1600[3]	127[3]	127[3]
McIntyre & Anderton[27]	rigid polyurethane	1200[29]	1600[3]	127[3]	127
Fowlkes (1974)[28]	rigid polyurethane	1200[29]	1600[3]	127[3]	127
Thornton and Magee[21]	aluminium			52.2	-
	Al 7 % Mg }	2700[17]	69000	229	-
	Al 7075			342	
Thornton and Magee[22]	Zn at -196 °C	5200	43000	---	207[22]
Walsh et al.[17]	glass	2511[17]	75000[17]	---	
Pittsburg-Corning[18]	glass	2500[34]	7000[34]	---	

TABLE 3: THE EQUATIONS FOR STIFFNESS AND STRENGTH OF FOAMS

PROPERTY	OPEN CELLS FOAMS*	CLOSED CELL FOAMS†
LINEAR ELASTICITY	$\frac{E}{E_s} = C_2 \left(\frac{\rho}{\rho_s}\right)^2$ $C_2 \approx 1$ (eqn.5)	$\frac{E}{E_s} = B_2 \left(\frac{\rho}{\rho_s}\right)^3$
ELASTIC COLLAPSE	$\frac{\sigma^*_{el}}{E_s} = C_3 \left(\frac{\rho}{\rho_s}\right)^2$ $C_3 \approx 0.05$ (eqn.7)	$\frac{\sigma^*_{el}}{E_s} = B_3 \left(\frac{\rho}{\rho_s}\right)^3$
PLASTIC COLLAPSE	$\frac{\sigma^*_{pl}}{\sigma_y} = C_4 \left(\frac{\rho}{\rho_s}\right)^{\frac{3}{2}}$ $C_4 \approx 0.3$ (eqn.9)	$\frac{\sigma^*_{pl}}{\sigma_y} = B_4 \left(\frac{\rho}{\rho_s}\right)^2$
BRITTLE CRUSHING	$\frac{\sigma^*_f}{\sigma_f} = C_7 \left(\frac{\rho}{\rho_s}\right)^{\frac{3}{2}}$ $C_7 \approx 0.65$ (~~eqn.~~13)	$\frac{\sigma^*_f}{\sigma_f} = B_7 \left(\frac{\rho}{\rho_s}\right)^2$

*In most foams the solid is concentrated into the cell edges; then the open-cell formulae are appropriate. The maps shown in Figs.15 and 17 were constructed using them.

†These equations refer to true, closed-cell foams with no thickening of the cell edges. They are derived by the method given in the text, but using eqn.(3) in place of eqns.(1) and (2). The quantities B_1 to B_2 are dimensionless constants.

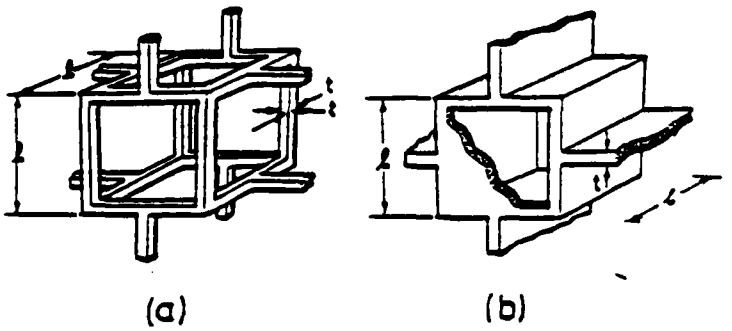

Fig. 1 The 3-dimensional structure of open and closed-cell foams, idealised. The cell walls meet so that loads cause bending moments to be applied to the cell walls. Most foams behave like the open-cell foam.

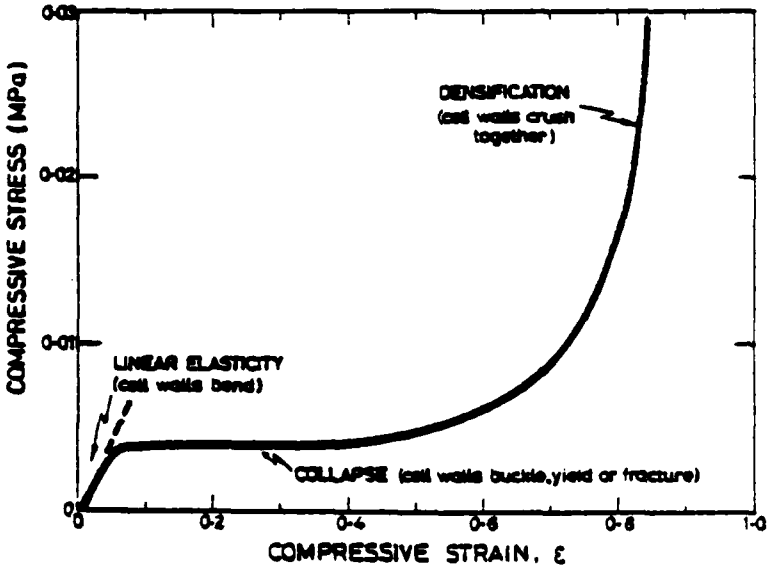

Fig. 2 The typical shape of the stress-strain curve for a foam.

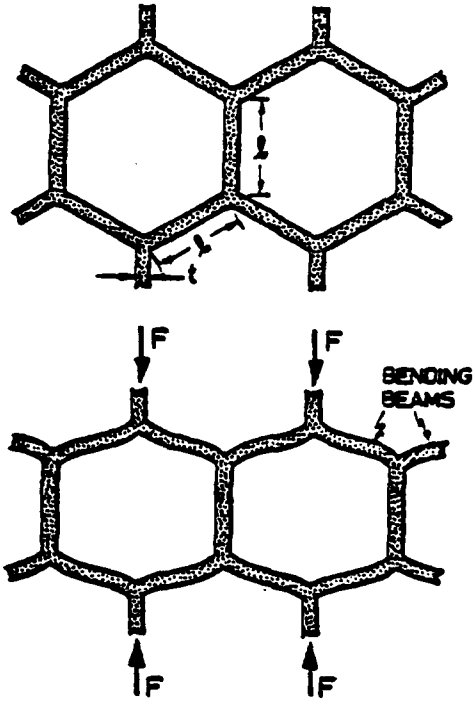

Fig. 3 The linear-elastic deformation of a foam: the cell walls bend so that the bending deflection δ is proportional to the force F.

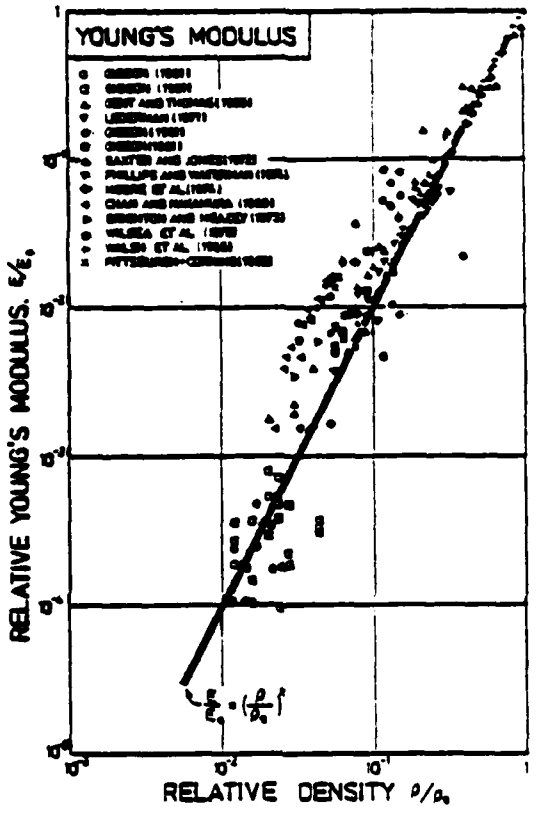

Fig. 4 The relative Young's modulus, E/E_s, plotted against relative density, ρ/ρ_s. Open symbols represent open-cell polymer foams; shaded symbols represent closed-cell polymer foams, crosses are ceramic and glass foams. (The references, in order, are: 1,5,8,11-17; normalising constants in Table 2.)

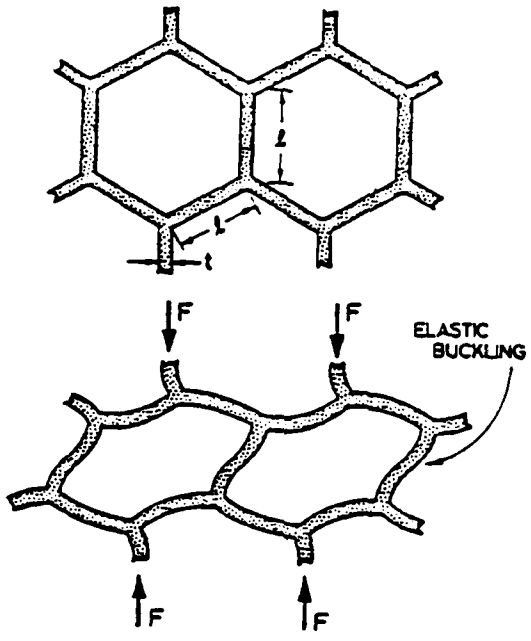

Fig. 5 The non-linear deformation of a foam: the cell walls buckle, giving large deformation at an almost constant stress.

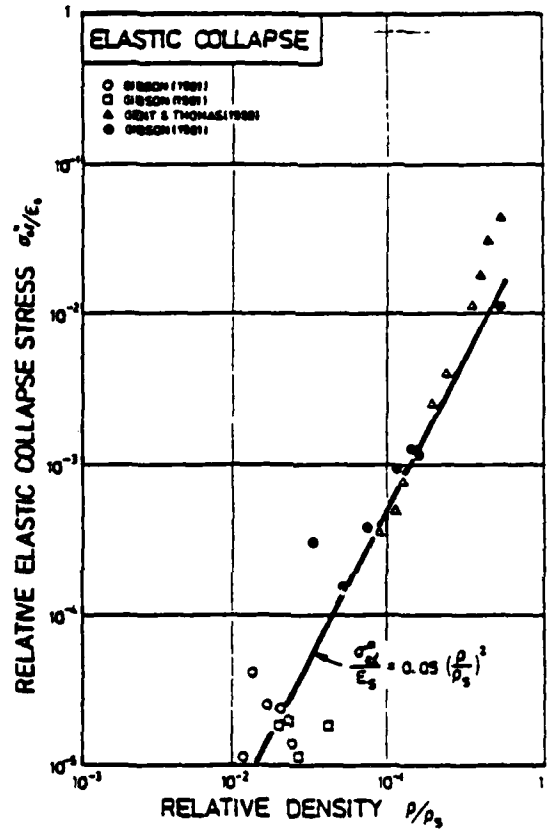

Fig. 6 The relative elastic collapse stress, σ^*_{el}/E_s, plotted against relative density, ρ/ρ_s. Open symbols represent open-cell polymer foams; shaded symbols represent closed-cell polymer foams. (The references, in order, are: 1,5; normalising constants in Table 2.)

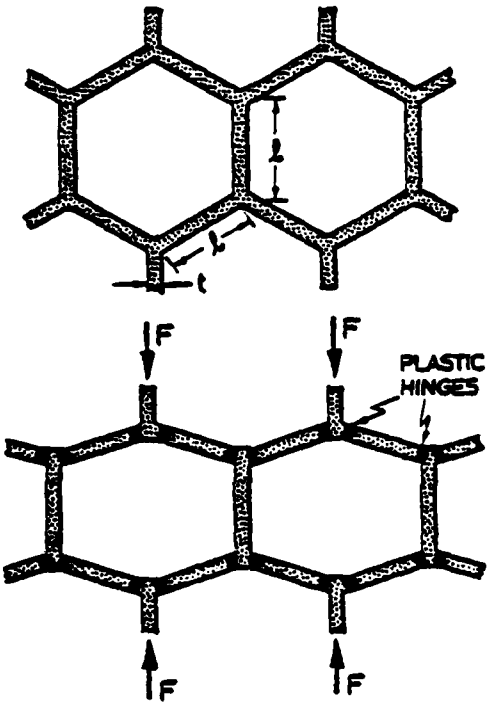

Fig. 7 The yielding of a plastic foam: the fully plastic moment of the cell wall is exceeded, giving large deformation at an almost constant stress σ^*_{pl}.

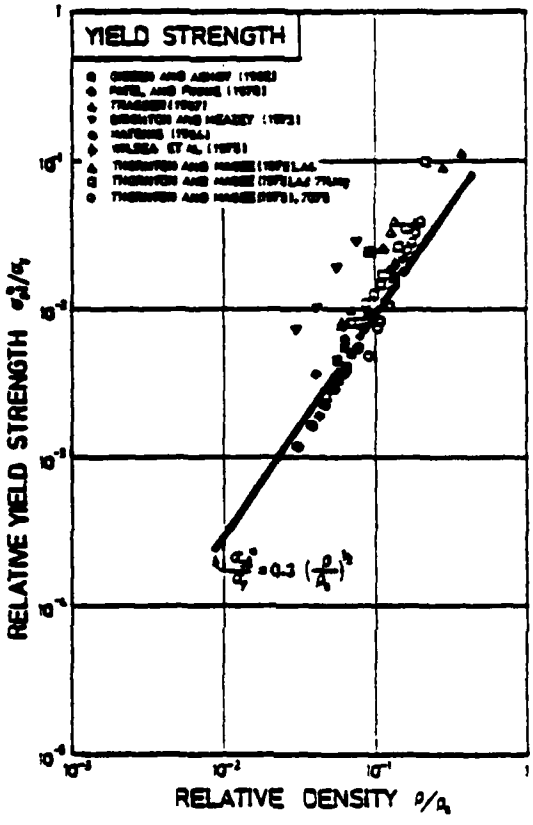

Fig. 8 The relative plastic collapse stress, σ^*_{pl}/σ_y, plotted against relative density, ρ/ρ_s. Open symbols are for metal foams; shaded symbols are for closed-cell polymer foams. (The references, in order, are 10,3,23,15,19,16,21; normalising constants in Table 2.)

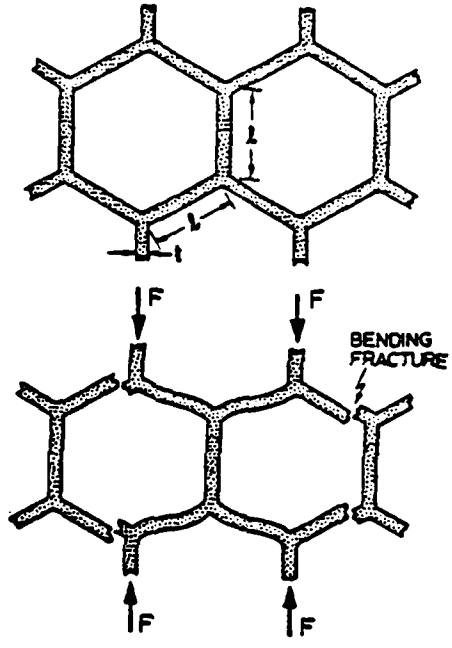

Fig. 9 The crushing of a brittle foam: the modulus of rupture of the cell walls is exceeded, causing them to fracture.

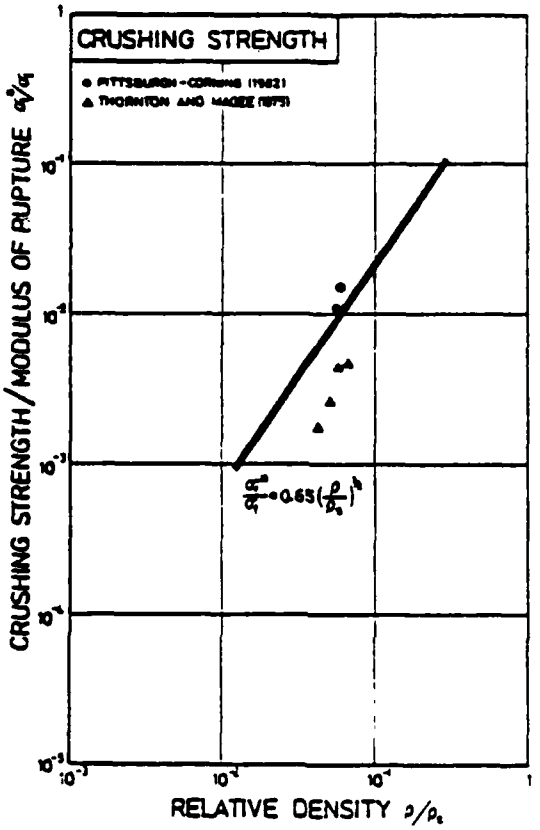

Fig. 10 The relative crushing strength, σ_f^*/σ_f, plotted against relative density ρ/ρ_s, for brittle foams. (The references, in order, are: 18,22; normalising constants in Table 1.)

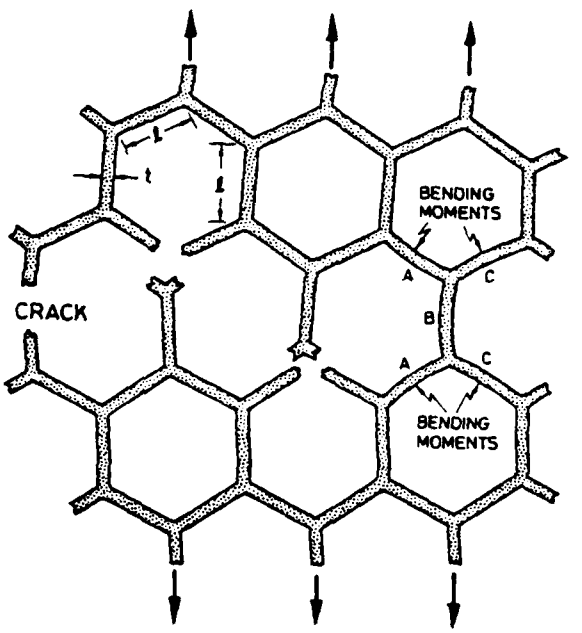

Fig. 11. Mode 1 crack propagation in a brittle foam: the field of the crack subjects cell walls to a bending moment and to tension. When the breaking strength of the cell wall is exceeded, the crack propagates.

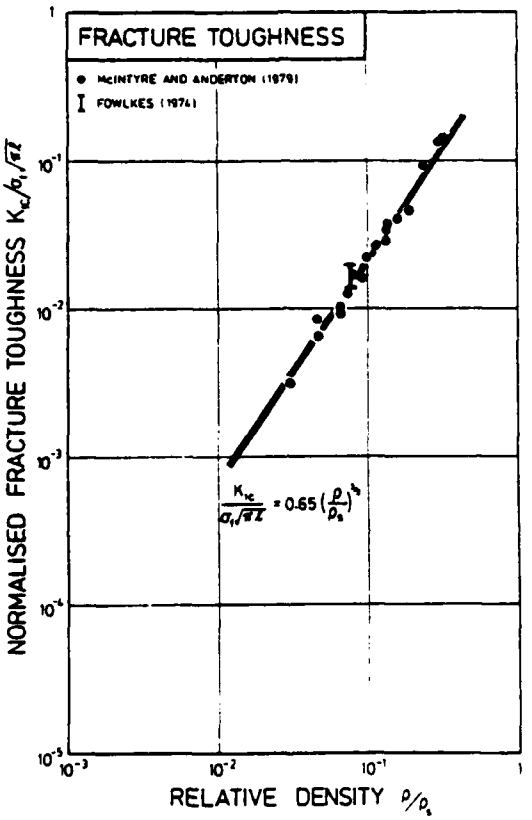

Fig. 12. The normalised fracture toughness $K_{IC}/\sigma_f \sqrt{\pi \ell}$ plotted against ρ/ρ_s for crack propagation in brittle foams. The references, in order, are: 27,28; normalising constants in Table 2.)

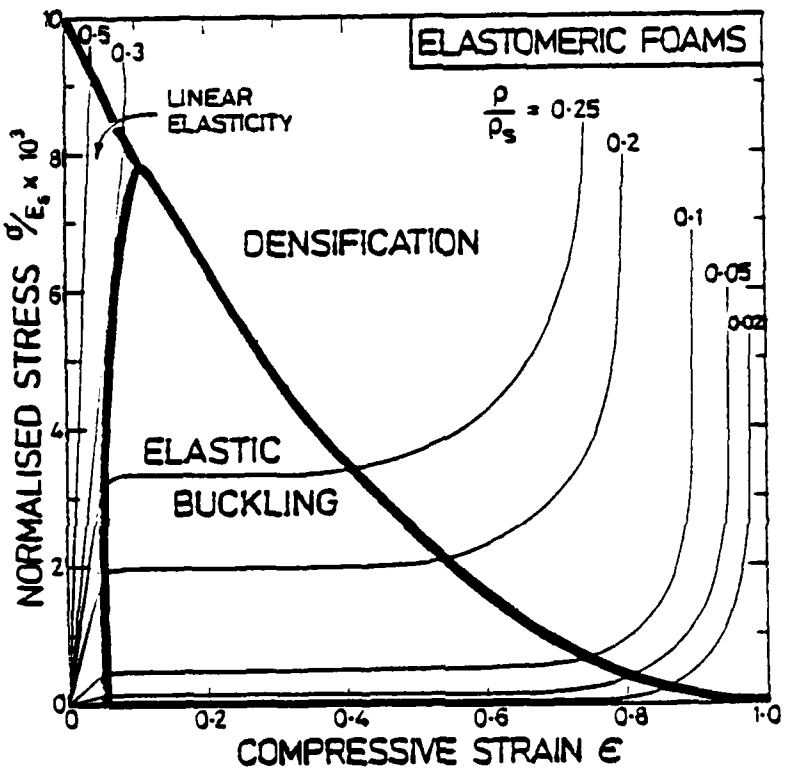

Fig. 13. A deformation-mechanism map for elastomeric foams, for relative densities from 0.02 to 1.

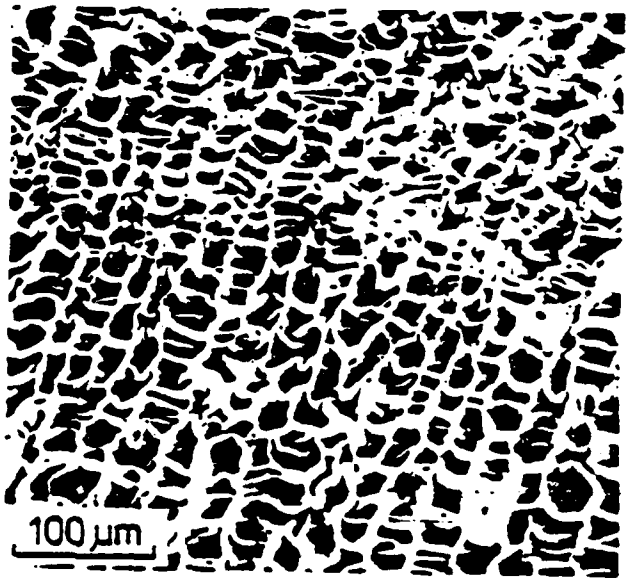

Fig. 14. The progressive collapse of cork, an elastomeric foam.

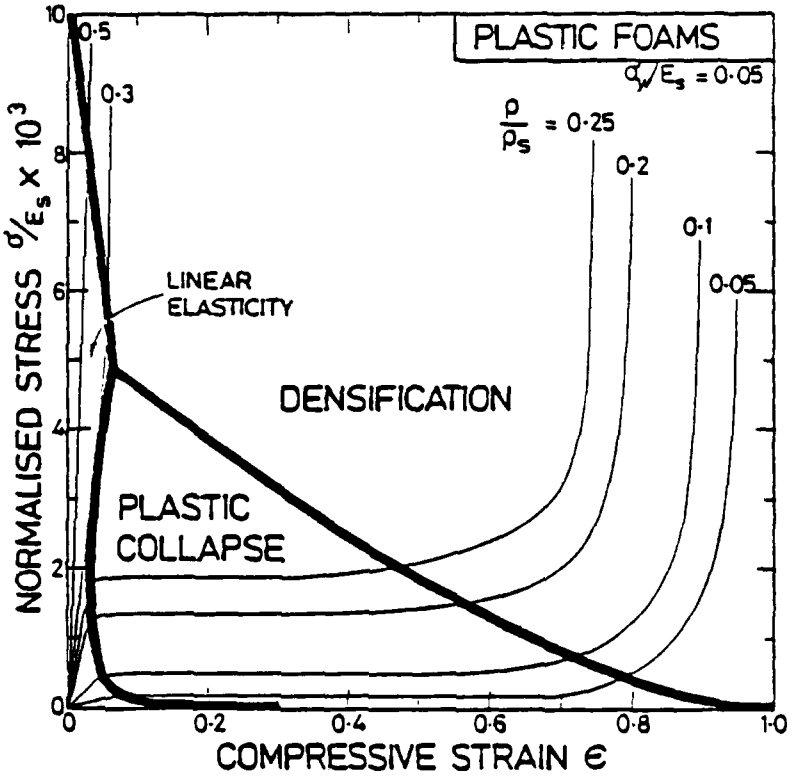

Fig. 15. A deformation-mechanism map for a plastic foam, for which $\sigma_y/E_s = 0.05$, for relative densities from 0.05 to 1.

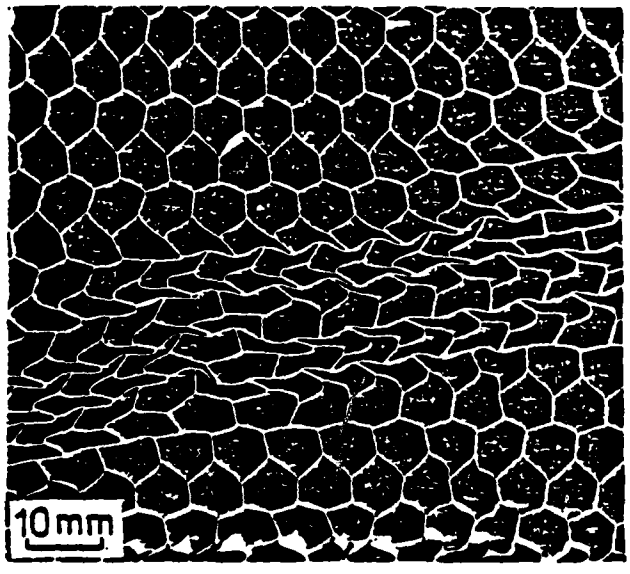

Fig. 16. The progressive collapse of cells in an aluminium honeycomb.

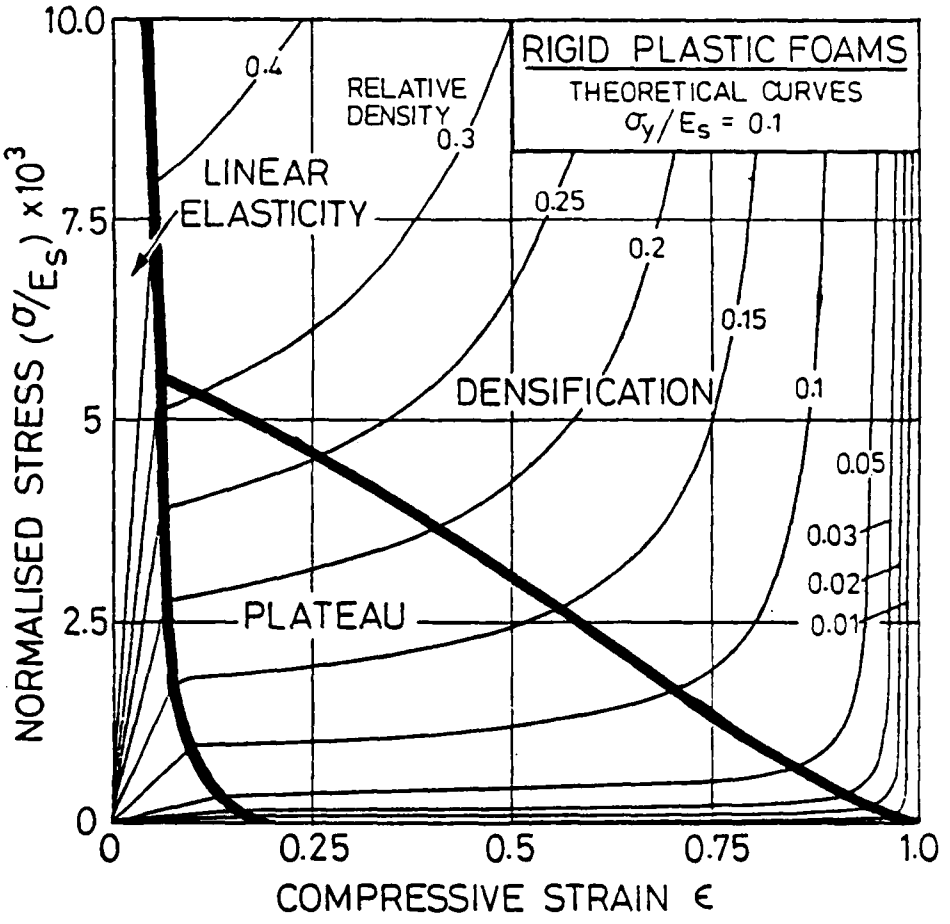

Fig. 17. A deformation-mechanism map for a rigid plastic foam, for which $\sigma_y/E_s = 0.1$, for relative densities from 0.01 to 1.

PART 2 DEFORMATION MAPS FOR SOLID POLYMERS

Summary

Data for the viscoelastic modulus can be presented as diagrams which summarise how the modulus depends on temperature and time. The diagrams are useful as a way of classifying polymers by the mechanical response and in summarising information about the mechanisms of deformation of the polymer, and in presenting design data in an easily accessible way.

1. INTRODUCTION

A number of deformation regimes can be identified for a given class of polymers. A linear polymer such as PMMA shows 4 distinct regimes, each characterised by a certain range of modulus:

(a) Glassy behaviour at $T < T_g$, characterised by a Young's modulus of around 4 GPa .

(b) Viscoelastic behaviour close to T_g, described by a coupling of the W L F viscosity with a suitable elastic modulus, leading to a time-dependent viscoelastic modulus between 1 and 10^3 MPa .

(c) Rubber elasticity at $T > T_g$, caused by entanglements, following Hooke's law, with a modulus around 1 MPa .

(d) Viscous flow at temperatures well above the glass temperature, following a simple viscous flow law.

We have made a preliminary examination of the range of operation of each of these mechanisms, and the models which have been developed to describe them, with a view to assembling the information into maps. One possible choice of axes are the *viscoelastic modulus* E and *normalised temperature* $\bar{T}$, where:

$$E = \frac{\sigma}{\varepsilon^{TOT}}$$

where σ is the stress, ε^{TOT} is the total strain accumulated in a time t and

$$\bar{T} = T/T_g$$

where T_g is the glass temperature (Fig.1). The temperature axis runs from $\bar{T} = 0$ to $\bar{T} = 2$, and the modulus axis from 10^{-3} to 10^4 MPa . This is not the only possible way of presenting the results, but it is one that nicely displays the regimes of glassy, viscoelastic and rubbery and viscous behaviour.

2. THE GLASSY MODULUS

Amorphous polymers below their glass temperature have moduli around $4\ GN/m^2$. These low values reflect the stretching of the relatively weak van der Waals bonds which bind one chain to another, and by rotation about certain carbon-carbon bonds in the chain backbone such as to elongate the molecule in the direction of loading (Bowden, 1968; Yannos and Luise, 1982). The stretching and bending of the carbon-carbon bonds requires much higher forces, and do not contribute in an important way to the modulus. If the internal energy of the polymer, per unit volume, is $V(\varepsilon)$, then Young's modulus can be calculated from the change in V with tensile strain, ε :

$$E = \frac{d^2V}{d\varepsilon^2} \tag{1}$$

The intermolecular van der Waals bonds arise from dipole-dipole induction and dispersion forces and bind one polymer chain to its immediate neighbour. It is a short-range interaction, well modelled by a Lennard Jones potential:

$$V(\varepsilon) = V_o \{(\frac{a_o}{a})^{12} - 2(\frac{a_o}{a})^6\} \tag{2}$$

where $\varepsilon = \frac{a-a_o}{a_o}$. Substituting and differentiating, we obtain:

$$\frac{dV}{d\varepsilon} = 12\ V_o \{(\frac{1}{1+\varepsilon})^{13} - (\frac{1}{1+\varepsilon})^7\}$$

$$\frac{d^2V}{d\varepsilon^2} = -12\ V_o \{13(\frac{1}{1+\varepsilon})^{14} - 7(\frac{1}{1+\varepsilon})^8\} \tag{3}$$

$$= -36\ V_o$$

The second major contribution to the elastic deformation arises from bond rotation. Polarised infrared spectroscopy on samples of glassy polycarbonate (PC), annealed below the glass transition temperature, gives direct evidence for the rotation of segments of a chain about a carbon-carbon bond. The bond rotations are modelled by a 3-link deforming unit (Bowden, 1968; Yannos, 1974) or "strophon". Rotation of the middle link causes an overall change in length. For rotation to take place, the hindrance caused by the sidegroups must be overcome. This has been modelled by a two-fold symmetric potential (Flory, 1969):

$$V(\phi) = \frac{V_o}{2} \{1 - \cos n\ (\phi - \phi_o)\} \tag{4}$$

Using this idea, Yannos and Luise (1982) have calculated the contributions of inter- and intra-molecular forces to the glassy modulus at 0 K for six different amorphous polymers. The relative contribution of the two deformation modes depends on the length of the strophon links: the longer the link the more difficult it is for the bond to rotate, causing intermolecular forces to become more dominant. This may explain the contention between Bowden (1968), who proposes *intramolecular* forces are dominant in the modulus of a glassy polymer using polyethylene (PE) data and Yannos (1974) who proposes *intermolecular* forces are dominant, based on PC data. PC has longer strophon links than PE.

Although such models allow an estimate of the modulus at 0 K , they are insufficiently precise for our purposes. Instead, we use values of E_o obtained by extrapolating measurements of E at higher temperatures, to 0 K .

Increasing the temperature has two distinct effects. First, thermal expansion increases the molecule separation and lowers the van der Waals restoring forces and the forces opposing rotation about carbon-carbon bonds: this gives a slow drop in modulus, but does not introduce a rate-dependence. Second, the thermal energy of the molecules now makes local, thermally activated, rearrangements possible, giving extra (time-dependent) strain, and an associated drop in modulus. The first effect (thermal expansion) leads to a roughly linear decrease in modulus with temperature. Yannos and Luise (1982) develop this idea, taking account of thermal expansion: increase in temperature increases the interchain distance, reducing the force required for *intermolecular* deformation. The results, even for this one contribution, are complex, but simplify (to within ±10%) to:

$$E = E_o \left(1 - \alpha \frac{T}{T_g}\right) \qquad (5)$$

where

$$\alpha = \frac{T_g}{E_o} \frac{dE}{dT}$$

It is reasonable to assume that the rotational contribution behaves in a similar way, so that eqn.(5) describes the effect of thermal expansion on modulus. Lee et al. (1975) review data for moduli of glassy polymers and conclude that they are well described by a linear temperature dependence (eqn.5). Van Krevelen (1976) finds a better fit to the empirical relation:

$$E = E_o/(1 + 2\ T/T_g) \qquad (6)$$

which reduces to eqn.(5) (with $\alpha = 2$) for low temperatures, but which gives a steeper drop near T_g .

The second contribution derives from the thermally activated motion of side groups, or of short segments of chains, past each other, giving a little extra strain. This thermally activated relaxation is difficult to model because, at low temperatures, only a few sites with the lowest activation energy, Q , can move; at a higher temperature, more sites with higher Q become mobile. This spectrum of activation energies leads to cumbersome equations. We adopt the view that polymers below T_g exhibit *secondary transitions* in addition to the main glass-rubber transition. Below the glass transition, there remains some limited freedom of rotation or sliding either of short segments or side groups. The energy involved in these transitions is lower than that for full movement, so they occur at lower temperatures. If we assume, for one such process, a *single* activation energy Q , then if the relaxation time at a standard temperature T* is τ^* , then at any other temperature T, τ is given by:

$$\tau = \tau^* \exp \frac{Q}{R} \left(\frac{1}{T} - \frac{1}{T^*}\right) \tag{7}$$

The total strain resulting from pure elastic deformation plus a visco-elastic contribution that is due to the transition, at constant stress, is:

$$\varepsilon = \frac{\sigma}{E} \left(1 + \frac{\Delta E}{E} \left(1 - \exp - \frac{t}{\tau}\right)\right) \tag{8}$$

where E is given by eqn.(1). Thus, the relaxation can be included, provided four pieces of information are known: the activation energy Q , the amplitude of the relaxation $\Delta\varepsilon/\varepsilon$ and the relaxation time τ^* at temperature T* . Further relaxations can be included by adding further terms like that given above.

3. THE GLASS-RUBBER (OR VISCOUS) TRANSITION

When sufficient thermal energy is available, the van der Waals bonds holding the molecular chains of a polymer together start to melt. This enables segments of the once elastically-bonded chains to undergo large sliding movements relative to each other, introducing an element of viscous flow into the deformation of the polymer. This appears as a reduced modulus.

In an amorphous polymer, a single empirical function can describe

the temperature dependence of the mechanical relaxation near the glass transition. Williams, Landel and Ferry (1955) describe the ratio of the mechanical relaxation time τ, at temperature T to the value τ_s at a reference temperature T_s (with suitable choice of T_s) by

$$\log\left(\frac{\tau}{\tau_s}\right) = \frac{-C_1(T-T_s)}{C_2 + (T-T_s)} \tag{9}$$

where $T_s = T_g + 50^o$. If T_g is chosen as the reference temperature, then we find

$$\log\left(\frac{\tau}{\tau_g}\right) = \log\frac{\eta(T)}{\eta(T_g)} = \frac{-17.44(T-T_g)}{51.6 + (T-T_g)} \tag{10}$$

or

$$\eta(T) = \eta(T_g)\exp-\frac{7.57(T-T_g)}{51.6 + (T-T_g)} \tag{11}$$

Note that eqn.(11) implies that both the viscosity and activation energy for viscous flow become infinite at $T = T_g - 51.6^o$.

The prediction is that all molecular motion should become completely frozen at $T < T_g - 51.6$. What happens, of course, is that new mechanisms of deformation take over; for example relaxation of the carbomethoxy side chain at about 20^oC and the aliphatic ester group at $T < 150^oC$ for PMMA.

Using the above formulation data obtained (for example) at different temperatures but at similar times can be shifted to coincide on the time scale to produce a 'master curve' at a chosen temperature. One such 'master curve' is produced by McLoughlin and Tobolsky (1952) from stress relaxation data of PMMA (Figs.1 and 2).

Other theories have been developed to account for the temperature dependence of viscosity in the glass transition region. They include *barrier theories* using potential wells and *statistical theories* considering enthalpy (see Arridge 1975 for a short review). But the WLF equation has been the most successful over the temperature range T_g to $T_g + 100$ K. Although it was put forward as an empirical equation, it has some physical basis. Consider the 'free volume' of a polymer system. The free volume, V_f, can be thought of as the difference between the total volume V and that occupied by the atoms when densely packed, V_o. The total volume V is assumed to be that of packed cylinders with a radius equal to the van der Waals radii around the chains (V_o), plus that volume associated with vibrational

motion. The free volume $(V-V_o)$ is "free" in the sense that it can redistribute, continuously, due to thermal motion. It provides the extra volume required for larger scale motion. Experimentally, the occupied volume increases linearly with temperature whereas the total volume shows a discontinuity at $T = T_g$ (Fig.3). Doolittle (1951, 1952) has shown that

$$\eta = \eta^* \exp(\frac{B}{f_V}) \tag{12}$$

where η^* is the viscosity at some standard state and f_V is the fractional free volume $(V-V_o/V)$. Assuming a linear dependence of fractional free volume above T_g with temperature we find

$$f_V = f_g + \alpha_f(T-T_g) \qquad (\text{at } T \geq T_g)$$

where α_f is the volume expansion coefficient, from which

$$\ell n(\frac{\eta(T)}{\eta(T_g)}) = \frac{-B/f_g(T-T_g)}{f_g/\alpha_f + (T-T_g)} \tag{13}$$

which is equivalent to the WLF equation with

$$C_1 = B/2.3\, f_g \qquad \text{and} \qquad C_2 = f_g/\alpha_f$$

where f_g is the fractional free volume at T_g .

We include this information into the maps in the following way. Consider the rheological model shown in Fig.4. It describes the bond-stretching elasticity by the spring E_1 , the viscous sliding of molecules (as given by the WLF equation) by the dashpot $\eta(T)$ and the rubbery modulus by the spring E_2 . The full constitutive law for this standard linear model is

$$\varepsilon + \frac{E_2}{\eta}\varepsilon = \frac{\sigma}{E_1} + \frac{\sigma}{\eta}(\frac{E_1+E_2}{E_1}) \tag{14}$$

At *constant load (creep)* the solution is

$$\varepsilon = \sigma\{\frac{1}{E_1} + \frac{1}{E_2}(1 - \exp - \frac{E_2}{\eta}t)\}$$

Then the apparent modulus σ/ε , for loading time t at temperature T is

$$E'_{C.L.} = \frac{E_1}{1 + \frac{E_1}{E_2}\{1 - \exp - \frac{E_2}{\eta}t\}} \tag{15}$$

This correctly goes to E_1 for short times and low temperatures, and to $E_1E_2/(E_1+E_2)$ for long times and high temperatures.

Under *constant strain* (stress relaxation) the result is slightly different. We have instead

$$\sigma + \frac{\sigma}{\eta}(E_1+E_2) = \frac{E_1E_2}{\eta}$$

The solution is

$$\sigma = E_1\varepsilon\{1 - \frac{E_1}{E_1+E_2}(1 - \exp - \frac{E_1+E_2}{\eta}t)\}$$

and the apparent modulus is

$$E'_{C.S.} = E_1\{1 - \frac{E_1}{(E_1+E_2)}(1 - \exp - \frac{(E_1+E_2)}{\eta}t)\} \qquad (16)$$

As before, $E'_{CS} = E_1$ when time is short or temperature is low; and $E'_{CS} = E_1E_2/(E_1+E_2)$ when time is long or temperature high. But the transition between the two is different.

We now identify $E_1(T)$ with the glassy modulus, $E_2(T)$ with the rubbery modulus, and $\eta(T)$ with the WLF equation. The apparent modulus is calculated and plotted using either eqn.(15) or eqn.(16).

4. THE RUBBERY MODULUS

Above T_g, amorphous polymers may exhibit a rubbery modulus plateau of around 1 MN/m^2. This value is close to that of crosslinked rubbers and arises in a similar way.

The molecular chains in the polymer form a network by curling and twisting around each other forming mechanical entanglements which behave rather like the chemical branch points of a crosslinked polymer. These are called entanglements and a polymer in this region of behaviour is characterised by an average molecular weight between entanglements, $\bar{M}_e$. As the molecular weight, M_w, increases and so more entanglements take place, $\bar{M}_e$ is reduced and a higher rubbery modulus observed.

To predict the modulus, the entanglement network is assumed to act like a crosslinked network. When the polymer is strained, the entanglement points constrain the free slippage of molecules relative to each other, and the molecular network tends to align, reducing its entropy. The resistance to this ordering results in the modulus of the rubbery region.

Standard texts (Treloar 1958, Ward 1970) give a derivation of the rubbery modulus E_R for small strain. It is found that:

$$E_R = \frac{3 \rho RT}{\bar{M}_e} \tag{17}$$

where ρ is the density, T the absolute temperature and R the gas constant. This equation has been used to calculate the rubbery plateau on the maps.

5. NEWTONIAN-VISCOUS FLOW

At high temperature ($T > 1.2\ T_g$) the van der Waals bonds have completely melted, and even the entanglement points slip relatively easily. At low shear rates the polymer flows in a Newtonian viscous manner.

Apart from the chemical dependence of viscosity, which will not change for a specified polymer system, the viscosity is dependent on molecular weight $\bar{M}_w$ and the temperature T. The dependence of the viscosity on $\bar{M}_w$ is given by (van Krevelen, 1976):

$$\begin{aligned} \log \eta_o &= \log \eta_{cr} + 3.4 \log(\bar{M}_w/M_{cr}) \quad (\text{if } \bar{M}_w > M_{cr}) \\ \log \eta_o &= \log \eta_{cr} - \log(M_{cr}/\bar{M}_w) \quad (\text{if } \bar{M}_w < M_{cr}) \end{aligned} \tag{18}$$

The temperature dependence of viscosity is given by:

$$\eta_o = \eta^* \exp(Q/RT) \tag{19}$$

The WLF equation can be combined with eqn.(18) to give, for low shear rates,

$$\log \eta_o = \log \eta_{cr} + 3.4 \log(\bar{M}_w/M_{cr}) - \frac{17.44(T-T_g)}{51.6 + (T-T_g)} \tag{20}$$

Data are readily available to describe Newtonian flow, although large variations can be found between different investigations.

5.1 *Data for PMMA*

Data from van Krevelen (1976) given in terms of $\eta_{cr}(T)/\eta_{cr}(1.2\ T_g)$ are converted for $M_w = 100{,}000$ using eqn.(18), $\eta_{cr}(1.2\ T_g) = 1.26 \times 10^3\ Ns/m^2$ and $M_{cr} = 30{,}000$, also from van Krevelen.

It is found that the activation energies Q (in eqn.(19)) are similar, 157 kJ/mol for Diakon and 136 kJ/mol for van Krevelen's data.

The value η^* (eqn.(19)) is dependent on the molecular weight but can be calculated given a value of viscosity at a known temperature T thus:

$$\eta^* = \{\log \eta_{cr}(T) + 3.4 \log(M_w/M_{cr})\}/\exp(\frac{Q}{RT}) \qquad (21)$$

The apparent modulus is then calculated from

$$E = \frac{\sigma}{\varepsilon_{TOT}} = \frac{\sigma}{\varepsilon t}$$

or

$$E = \frac{\eta}{t} \qquad (22)$$

6. CONSTRUCTION OF THE MAPS

The maps are constructed from eqns.(15) and (16) together with eqn.(22). For each temperature, the modulus corresponding to a given loading time t is calculated and plotted as shown in Fig.5. Modifications of the equations give the modulus associated with cyclic loading. We find that, to give a good fit to the data, the time constant in eqns.(15) and (16):

$$\tau = \frac{\eta}{E_2}$$

and

$$\tau = \frac{\eta}{E_1 + E_2}$$

requires modification, and we are now working on maps of doing this in a consistent way, and conducting a detailed comparison with experimental data.

7. CONCLUSIONS

Maps can be constructed which summarise the viscoelastic modulus of amorphous polymers $E(T,t)$ for a wide range of temperature T and time t. Several separate mechanisms are involved: bond stretching, constrained molecular sliding, rubbery behaviour, and true viscous flow. The work thus far must be thought of as a feasibility study, which indicates that the method has potential, and is worth developing further.

8. REFERENCES

Arridge, R.G.C. (1975) "Mechanics of Polymers", Clarendon Press, Ch.4.

Bowden, P.B. (1968) Polymer 9, 449-454.

Doolittle, A.K. (1951) J.Appl.Phys. 22, 1471.

Flory, P.J. (1969) "Statistical Mechanics of Chain Molecules", Interscience, New York, 1969.

ICI Technical Service Note, "Diakon", DN23, 4th Edition, June 1981.

Lee, C.S., Cadell, R.M. and Atkins, A.G. (1975) Int.Journ. of Fracture 11, 1052.

McCrum, N.G., Read, B.E. and Williams, G. (1967) "Anelastic and Dielectric Effects in Polymeric Solids", J. Wiley and Sons, London, Ch.3.

McLoughlin, J.R. and Tobolsky, A.V. (1952) J. Colloid Sci. 7, 555.

Sundararajan, P.R. and Flory, P.J. (1976) J.Amer.Chem.Soc. 96, 5025-5031.

Treloar, L.R.G. (1958) "The Physics of Rubber Elasticity", Clarendon Press, Oxford.

Van Krevelen, D.W. (1976) "Properties of Polymers", Elsevier, Amsterdam, Ch.15, Section B.

Ward, I.M. (1971) "Mechanical Properties of Solid Polymers", J. Wiley, London.

Williams, M.L., Landel, R.F. and Ferry, J.D. (1955) J.Amer.Chem.Soc. 77, 3701, 3.

Yannos, I.V. (1974) In Deformation in Glassy Polymers - Molecular Interpretation (Proc. IUPAC SYMP., Rio de Janiero), Elsevier, Amsterdam, 265-286.

Yannos, I.V. and Luise, R.R. (1982) J.Macromol.Sci.-Phys. B21(3), 443-474.

Yannos, I.V. and Lunn, A.C. (1971) Polymer Letters 9, 611.

Yoon, D.Y., Sundararajan, P.R. and Flory, P.J. (1975) Macromolecule 8, 776-783.

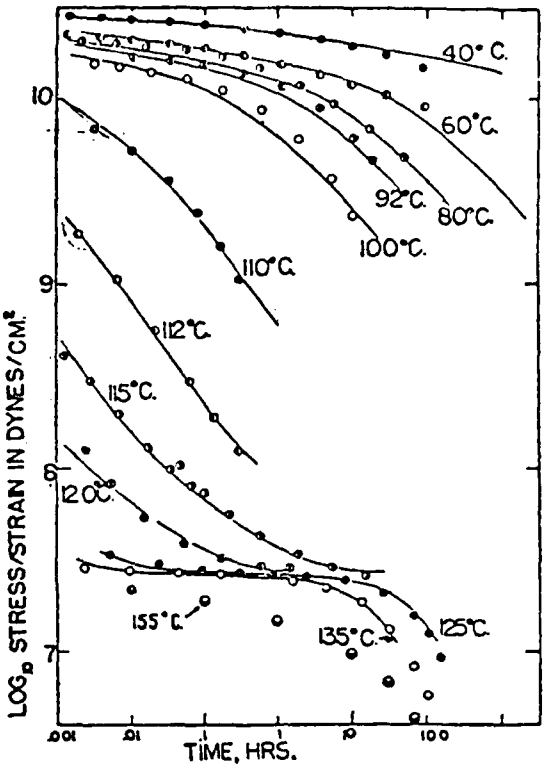

Figure 1. Comparison of experimental curves and master stress relaxation curve for polymethyl methacrylate.

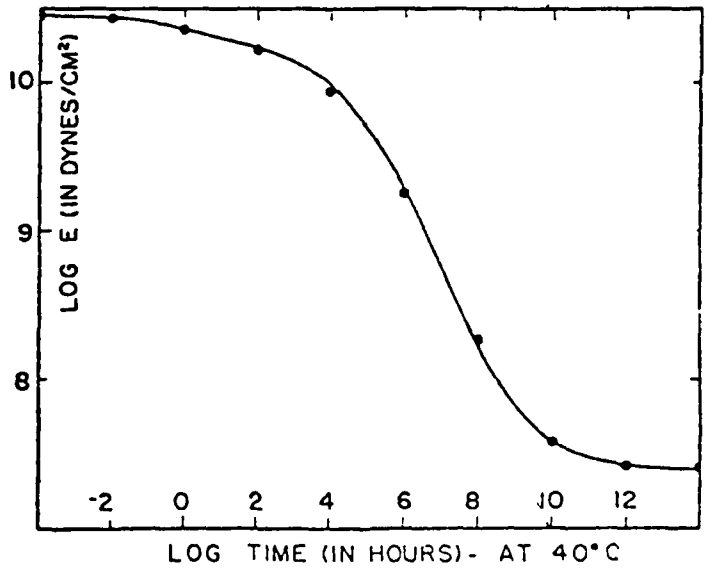

Figure 2. Comparison of master stress relaxation curve, calculated from the distribution of relaxation times.

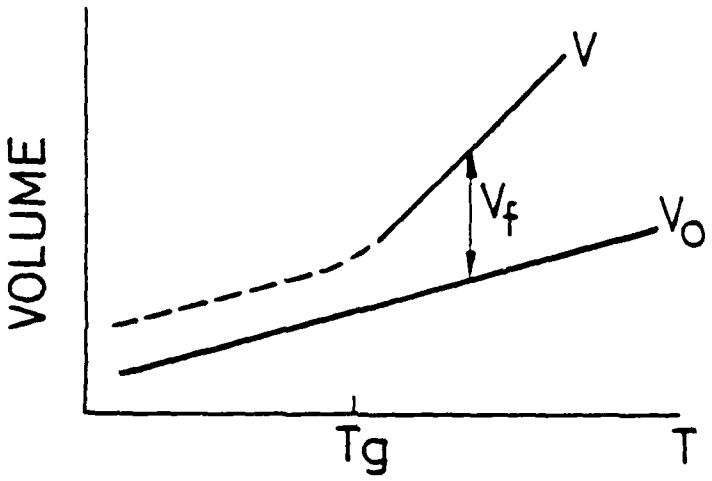

Fig. 3. Total volume V and occupied volume V_o as a function of temperature; the difference between the curves is the "free" volume.

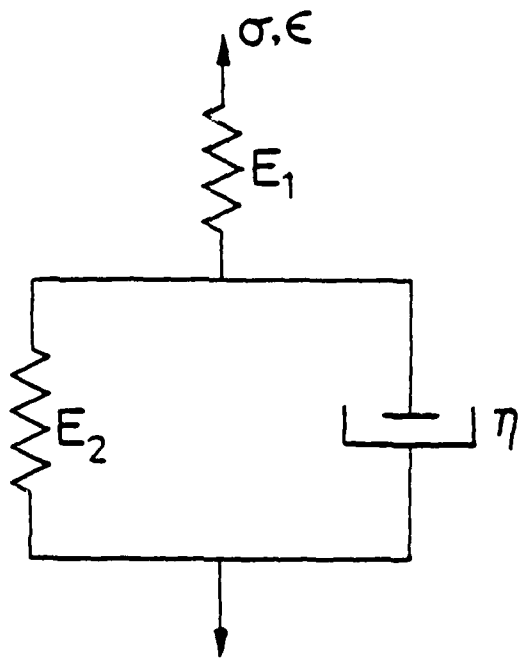

Fig. 4. Standard linear solid represented by a model of springs and dashpot.

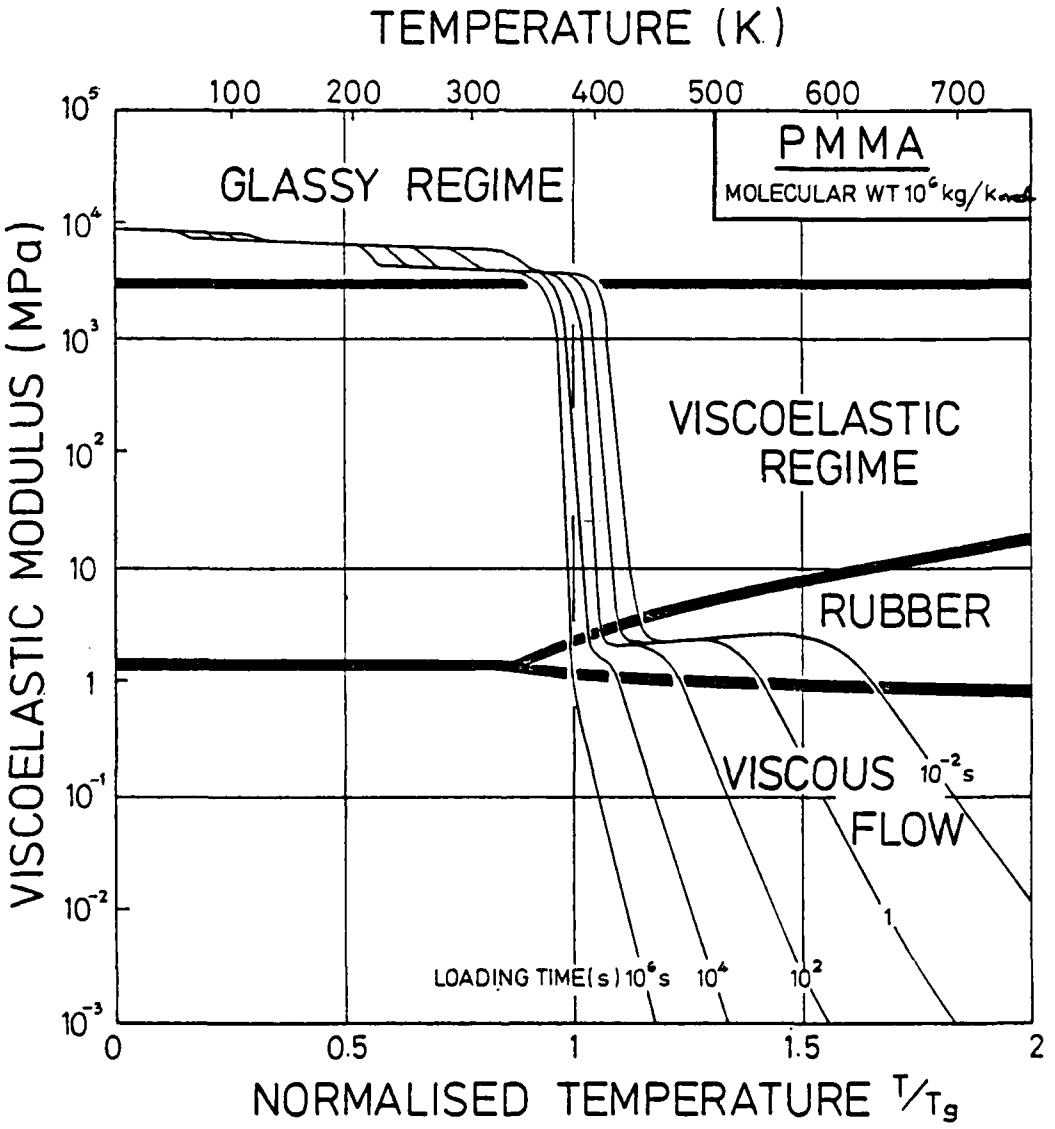

Figure 5. A deformation map for the glassy polymer PMMA.

PART 3 FRACTURE MAPS FOR POLYMER-COMPOSITES

Summary

The interaction between fracture mechanisms of a fibrous composite are complex. The effects of certain intrinsic material parameters, like the cohesive strength of the fibre-matrix interface or ductility of the matrix on the micromechanisms of fracture and toughness are unclear. One approach is to link our understanding of the failure processes with theoretical models of fracture to predict the toughness of a composite. However, the complex interactions between various intrinsic material parameters and a set of equations would not clearly be seen. Instead, we could construct maps based on these models to display information on fracture and toughness in a useful form. The fracture map would have two axes which are labelled using any two of the intrinsic material parameters that describe the fibre composite (Table 1). The map would be divided into areas or fields, each one depicting a particular failure mechanism. The boundary between one field and another would show a change in the dominant mechanism. Contour lines of predicted toughness could be superimposed onto the map in a manner useful for design and material selection.

1. INTRODUCTION

Polymeric materials containing long, strong fibres, fracture by a number of mechanisms. This section describes the principal mechanisms, and the construction of maps which show the important composite properties affecting these failure processes and the toughness. They are constructed from data of the properties of the fibre, matrix and interface, fitted to model-based equations of energy absorption which describe the mechanisms. Where experimental data is not available, for example, the misfit strain, ε_o , between fibre and matrix, we resort to theory to predict ε_o . Alternatively, where related data is available, for example, the interlaminar shear strength, we calculate values for the strength and toughness of a fibre-matrix adhesive bond using fracture mechanics relationships.

The first part of this section describes certain fracture mechanisms like fibre-matrix decohesion (debonding), fibre fracture and fibre pull-out and shows how to predict two important failure parameters, fibre* debond length, ℓ_d , and fibre pull-out length, ℓ_p . The second part shows how these predictions of fibre lengths can be combined with other model-based equations to estimate the energies dissipated for a number of fracture mechanisms. The third part shows how an estimation of these fracture energy terms can be displayed in the form of a fracture

*Throughout this section, the word 'fibre' is used to mean either an individual fibre or a bundle of fibres.

map to show the dominant mechanism of toughening and the predicted toughness for a particular set of material properties. A case study is carried out which shows how a map can be used to help identify the origins of hygrothermal aging phenomena.

The selection of maps presented is incomplete. They can be divided into three families of composite: glass fibres, carbon fibres and Kevlar fibres in epoxy resin. However, the method of analysing the fracture behaviour of fibrous composites and the construction of a map can be applied to other composite systems, short fibres in thermoplastic matrices, for instance.

1.1 *Fracture Mechanisms*

The fracture stress of a brittle solid like glass or graphite is not unique. It depends, for instance, on the distribution of flaw size in the sample. Most of the advanced fibres, carbon for instance, show a strength dependence on radius and length. The location of a fracture site along the length of an embedded fibre is also sensitive to the *rate* at which the load builds up in the fibre. This will depend upon the elastic properties of the fibre and matrix, modulus and Poisson's ratio, for example, and shear stress at the fibre-matrix interface. In a monotonic tensile test, the fibre is first likely to debond. The stress at which it does so is affected by the strength and toughness in shear of the fibre-matrix interface; also fibre modulus and radius. A complicated relationship therefore exists between the properties of the composite and the debond stress, σ_d , and fracture stress, σ_f ; and between σ_d , σ_f and two fibre lengths, the debond length and pull-out length.

Fibre debonding and fibre pull-out are the underlying failure processes which affect the fracture toughness of the composite. It is convenient to describe the failure processes in terms of the energy absorbed in creating new interfacial surface and the fracture and pulling-out of broken fibres from their matrix sockets. There are other energy terms that contribute to toughness; the stored elastic strain energy of the fibre, released when it snaps, matrix deformational energy, and surface energies of the fibre and matrix.* The mechanisms

*The energy associated with plastic flow in the matrix and fracture surface of the fibre and matrix is small compared to the total work to fracture the composite and will be ignored here.

of fibre debonding, fibre breakage and fibre pull-out are therefore related in complicated ways.

1.2 *Fracture Toughness Maps*

It would be useful to have some way of summarising, for a given composite system, information about the dominance of each mechanism and the important material properties affecting toughness. We have done this by constructing a map. It is a diagram with axes of any two of the composite parameters (there are at least 15 such variables, see Table 1). Fig.1 shows fibre strength plotted against fibre modulus for glass fibres in epoxy. The map is divided into *fields* which show the regions of fibre strength and fibre modulus over which each of the failure mechanisms is dominant. The letters PO = pull-out energy, EL = elastic (fibre) energy, and INT = interfacial surface energy.

The *field boundaries* are the loci of points at which two mechanisms are contributing equally to the toughness of the composite. Superimposed on the fields are *contours of constant toughness* (kJ/m^2): these show the predicted toughness of the composite by summing the contributions of each mechanism. Also displayed are *contours of constant fibre debond length and fibre pull-out length* (mm), two failure parameters useful in carrying out a failure analysis of a broken specimen. In constructing such a diagram, it is assumed that there are only two variables, and all of the other material parameters have fixed values. Such a map summarises, in a simple way, both the experimental and model-based understanding of the fracture of the composite in question.

2. DEBOND LENGTH AND PULL-OUT LENGTH EQUATIONS

In this section, we develop, with a brief explanation, the fibre debond length and pull-out length equations used later in the construction of the maps. First, we select for the debonding and then the pull-out of fibres, an equation which is based on a physically sound microscopic model of stress build-up in the fibre. While theory gives the form of the equation, we then resort to experimental data or simple ways of predicting the values of the parameters which appear in it.

2.1 *Fibre Debonding and Fibre Pull-Out*

When a unidirectional fibrous composite is loaded monotonically, the tensile stress on the fibre and the shear stress at the fibre-matrix interface both increase. It is likely, because of the low shear

strength of fibre-matrix interfaces, that the bond eventually fails. A cylindrical crack at the interface propagates along the fibre length. The process is called "debonding". If mechanical interaction between a debonded fibre and matrix is still possible, by fractional forces, for example, then load transfer to the fibre will take place. (Matrix shrinkage during fabrication and cooling may be the origin of such interaction, which sets up a radial compressive stress on the fibre.) This produces a non-uniform stress along the length of the debonded region. Because of the variability of strength, the fibre fractures at its weakest point. The eventual propagation of a macroscopic, transverse crack in a composite therefore produces a fracture surface showing protruded fibres of variable length, because of the variability of fibre strength. This process is called "pull-out" (Fig.2).

2.2 *Prediction of Fibre Debond Length*

The stress at which a fibre first debonds depends upon fibre modulus, E_f, fracture energy of the interface, G_{2c} (in shear), and fibre radius, r_f [1]:

$$\sigma_d = (4E_f G_{2c}/r_f) \qquad (1)$$

The frictional stress between a debonded fibre and matrix socket is related to the compressive radial stresses produced by the matrix during cooling and shrinkage, and the elastic properties of the fibre and matrix. The fibre stress can be described by[2]:

$$\sigma(x) = \sigma_p (1 - e^{-\beta x}) \qquad (2)$$

where x is distance from the tip of an interfacial crack, σ_p and β are functions of the elastic constants of the fibre and the matrix which take into account Poisson contraction of fibre under load:

$$\sigma_p = \varepsilon_o E_f/\nu_f \quad \text{and} \quad \beta = 2\mu\nu_f E_m/E_f r_f (1 + \nu_m)$$

E_m and ν_m are the modulus and Poisson ratio of the matrix, ν_f is Poisson ratio of the fibre and μ is the coefficient of friction at the interface, σ_p is proportional to the residual "misfit-strain", ε_o, between fibre and matrix, where $\varepsilon_o = \delta/r_f$ (δ is the difference in the radius of the matrix socket under stress-free conditions, and its enforced radius equal to r_f). Eqn.(2) shows the *rate* of stress build-up *decreases* as the load on the fibre *increases*. σ_p can

therefore be thought of as the maximum fibre stress that can be produced by frictional loading; i.e. when Poisson contraction of the fibre equals the residual strain in the adjacent matrix.

For a fibre that has debonded by an amount x, the fibre stress can therefore be written as:

$$\sigma(x) = \sigma_p - (\sigma_p - \sigma_d)\, e^{-\beta x} \tag{3}$$

Under monotonic loading, the interfacial crack spreads until the stress on the fibre reaches σ_f (Fig.3). The fibre debond length is therefore given by:

$$\boxed{\ell_d = 2\, \ell n\, |(\sigma_p - \sigma_d)/(\sigma_p - \sigma_f)|/\beta} \tag{4}$$

If $\sigma_d > \sigma_f$, no debonding occurs; if $\sigma_p > \sigma_f > \sigma_d$, then debonding spreads along the entire length of fibre.

The process of 'bundle debonding' can occur in preference to 'fibre debonding'. A bundle of fibres can be thought of as a 'large fibre' having the properties of the bundle. A bundle containing matrix between the fibres has properties similar to those of a uni-directional composite with $V_f \simeq 0.80$.

The interface toughness parameter, G_{2c}, in eqn.(1), is a linear function of two constituent material properties:

$$G_{2c} = |(\pi r_f G_1) + (a - 2r_f)G_2|/a \tag{5}$$

where G_1 and G_2 are the critical strain energy release rates for the fracture of interface and pure polymer respectively. The spacing between fibre centres, a, for a square packing array is:

$$a = (\pi r_f^2)^{\frac{1}{2}}/V_f \tag{6}$$

V_f is the volume fraction of fibres in the bundle.

For a typical epoxy, $G_2 = 500\ J/m^2$. We use the following G_1 values of 50, 2 and 60 J/m^2 for E-glass, Kevlar and high-strength carbon fibres, respectively. The misfit strain, ε_o, between bundle and matrix was claculated to be about 5%; the bundle radius, r_b, was of the order of 500 μm. Table 5 shows the predicted debond lengths based on the above values combined with eqns.(1), (4), (5) and (6).

2.3 *Prediction of Fibre Pull-Out Length*

Under monotonic loading, an embedded brittle fibre carrying a variable load along its length will either snap at a large flaw with a low stress or at a small flaw with a high stress. The fibre shown in Fig.4 will actually fracture at point A , away from the surface of a large crack, and pull-out. Its pull-out length depends upon the fibre stress distribution and the flaw size distribution along its length.

Under stress, σ , the fraction $P(\sigma)$ of a population of fibres that fail, in its simplest form, is:

$$P(\sigma) = 1 - e^{(-(\sigma/\sigma_o)^m)} \tag{7}$$

However, the probability of failure occurring in the i^{th} segment of a debonded fibre is *not* simply $P(\sigma_i)$. It also depends upon the probability that a more highly stressed section has not broken before the flaw in the i^{th} section has caused the fibre to snap. This is given by the sum of $1 - P(\sigma_j)$ for all $j > i$, i.e. all sections more highly stressed than section i . The relative probability of fracture occurring in section i can be given by an integral form of the cumulative probability function:

$$F(x) = \frac{\int_o^x P(\sigma(x')) \left(\int_{x'}^{\ell_d/2} 1 - P(\sigma(x''))dx''\right) dx'}{\int_o^{\ell_d/2} P(\sigma(x')) \left(\int_{x'}^{\ell_d/2} 1 - P(\sigma(x''))dx''\right) dx'} \tag{8}$$

The pull-out length is given by:

$$\ell_p = (\ell_d/2) - x \tag{9}$$

and $F(x')$ is the cumulative probability of x being less than x' . Consequently, the cumulative probability distribution of pull-out length being less than or equal to ℓ_p is:

$$1 - F|(\ell_d/2\ell - \ell_p)| \tag{10}$$

For composites, where $\sigma_d > \sigma_f$, no fibre debonding occurs. This is found in strongly-bonded systems like carbon fibres in epoxy. Individual fibre pull-out is not possible but 'bundle pull-out' can occur (we treat the bundle like a large diameter fibre where σ_d for the bundle is less than σ_d for the fibre; and σ_f for the bundle is about 80% of the individual fibre). The nature of pull-out is

therefore controlled by the debonding process. If separate fibres can debond, they will pull-out individually; glass and Kevlar fibres would be expected to do this. The distribution of pull-out can be determined from a knowledge of $P(\sigma)$ (eqn.7) and the fibre stress distribution (eqn.3). Evaluation of the integral (eqn.8) can be carried out using an analytical method or by a numerical technique. As a first approximation, the average pull-out length for glass fibres and Kevlar fibres in epoxy was found to be related to σ_d in a simple way:

$$\boxed{\bar{\ell}_p = \ell_d/6.8} \tag{11}$$

and for pulling out a bundle of carbon fibres by:

$$\boxed{\bar{\ell}_p = \ell_p/35} \tag{12}$$

3. FRACTURE ENERGY (TOUGHNESS) EQUATIONS

When a composite ply fractures, by the propagation of a crack from a pre-existing notch or hole, for example, a sequence of energy absorbing events occur in a region surrounding the notch-tip. For example, under increasing load, the matrix cracks, leaving intact fibres between the faces; the fibres debond and new interfacial surface is created; fibres snap at weak points and stored elastic energy is dissipated; and most broken fibres pull-out of matrix sockets doing work against friction at the interface (Fig.5).

3.1 Interfacial Surface Energy Equation

The surface energy of an interface is small, perhaps a few J/m^2. However, the area of debonded fibres and fibre bundles can be large and a significant amount of energy may be required to produce new surface. The contribution of the fibre (γ_1) and bundle (γ_b) to this toughening mechanism is additive and in proportion to the total area of debonded interface:

$$\boxed{G_i = (4\ell_{df}\gamma_1 V_f/r_f) + (4\ell_{db}\gamma_b/r_b)} \tag{13}$$

The effective bundle fracture energy is given by the weighted average of γ_1 and γ_2 :

$$\gamma_b = |(\pi r_f \gamma_1) + (a - 2r_f)\gamma_2|/a \qquad (14)$$

γ_2 is the work to fracture the matrix in shear.

3.2 *Fibre Elastic Energy Equation*

Under monotonic load, the elastic strain energy stored in a debonded fibre and matrix increases. When the fibre snaps, some of this energy is released in the form of heat, acoustic energy, etc. An estimation of the dissipated energy can be made from a knowledge of the stored energy in the fibre before and after fracture (Fig.6). The dissipated elastic energy is therefore the difference between the initial and final states of stress. The elastic energy stored in the debonded length of fibre immediately before the fibre snaps is:

$$U_i = 2 \int_o^{\ell_d/2} \pi r_f^2 |\sigma(x)|^2/2E_f \, dx$$

where

$$\sigma(x) = \sigma_p - (\sigma_p - \sigma_d)\, e^{-\beta x}$$

Assuming that after the fibre fractures the stress distribution is linear (Fig.6),

$$\sigma(x) = \sigma_m |1 - x/(\sigma_p - \sigma_d)|$$

then:

$$U_f = (\pi r_f^2/E_f) \int_o^{(\sigma_p - \sigma_d)} (\sigma(x)^2 dx = (\pi r_f^2/E_f)(\sigma_m^2(\sigma_p - \sigma_d)/3)$$

Therefore:

$$G_{el} = U_i - U_f$$

i.e.

$$\boxed{\begin{aligned} G_{el} = V_f \big| &(\sigma_p^2 \ell_d/2) - (\sigma_p - \sigma_d)^2 (e^{-\beta \ell_d} - 1)/2\beta \\ &+ 2\sigma_p(\sigma_p - \sigma_d)(e^{-\beta \ell_d/2} - 1)/\beta - (\sigma_m^2 \ell_d/6) \big| /E_f \end{aligned}} \qquad (15)$$

3.3 *Fibre Pull-Out Energy Equation*

The stress to pull a fibre out of its socket embedded at a distance x is:

$$\sigma(x) = \sigma_p (1 - e^{-\beta x})$$

and the work to pull-out a single fibre over a distance ℓ is:

$$w = \int \pi r_f^2 \sigma(x)\, dx$$

If the pull-out lengths have a uniform probability distribution, with an average of $\bar{\ell}_p$, then the average work of pull-out can be shown to be[2]:

$$\boxed{G_p = V_f \sigma_p \left| \bar{\ell}_p + (e^{-\beta \bar{\ell}_p} - 1)/\beta \right|} \qquad (16)$$

4. CONSTRUCTION OF THE MAPS

The failure mechanism which is *dominant* (meaning it contributes most to the total work to fracture the composite) depends on the properties of the fibre, matrix and interface. It is helpful, for a given composite system, to show the conditions under which each mechanism dominates and to display both the experimental data of toughness and predictions of the model-based equations. Such a diagram or "map" summarises, in a way which could not be achieved by examination of a series of equations, a model-based understanding of the fracture of composites, together with a display of experimental data. Ways of doing this were introduced briefly in Section 1.

4.1 *Method of Construction*

First, data for the material's properties are gathered; fibre strength and modulus, fibre diameter, matrix strength, modulus and toughness, interfacial shear strength and toughness, and so on. Second, we predict the fibre (and bundle) debond length, ℓ_d, and pull-out lengths, ℓ_p; also the frictional stress distribution parameters, σ_p and β, from the material properties. Third, values of ℓ_d and ℓ_p, together with appropriate values of the material properties, are inserted into the model-based equations to predict the energy dissipated for each micromechanism of fracture. Fourth, a computer constructs a map by allowing any of the material properties which affect a fracture

process, to be varied in turn along the two axes of the map, keeping all other material properties constant. The contours of constant toughness are obtained by summing the energy-based equations to give the total work to break the composite. Fifth, predictions of ℓ_d and ℓ_p are displayed as contours of constant length. Sixth, any experimental data plots of toughness and measurements of ℓ_d and ℓ_p are located on the appropriate map, if required.

Values of the parameters used for E-glass, Kevlar 49, high modulus and high strength carbon fibres are listed in Table 2. A selection of typical maps is shown in Figs.7-10.

4.2 *Comparison between Maps*

The predictions for typical composites, marked by a triangle, are summarised in Table 3. The models predict reasonable estimates of toughness, ℓ_d and ℓ_p, for all fibre systems despite the wide variation in fibre properties. In particular, the models predict the toughness of carbon fibre composites to be primarily due to the debonding of bundles of fibres, later pulled-out after fracture; and the toughness of Kevlar and glass fibre composites to be due to the debonding of individual fibres, later pulled-out after snapping. These predictions are observed in practice. The predicted toughness of Kevlar composites is high, principally due to fibre pull-out. In contrast, the fracture toughness of high modulus carbon fibre composites is low, derived from the debonding of fibre bundles. A summary of the predictions is displayed in Table 3, where the notation $\uparrow$ indicates an increase in toughness or fibre length with increasing material property.

4.3 *A Case Study*

Glass-epoxy laminates $|0/90|$ were fractured in 3-point bending after exposure to a hot, humid environment for up to 100 h. The toughness, G_c, was claculated and the fibre pull-out lengths were measured using an optical microscope. We observed a fall in toughness from 27 kJ/m^2 to 10 kJ/m^2, approximately. Fig.11 displays the experimental data on a facture map. We believe that the changes in toughness are principally due to variations in fibre strength and fibre-matrix misfit strain, which is read from the map. This implies that ε_o initially drops due to moisture induced swelling of the matrix. Degradation of fibre strength by moisture attack causes the large reduction in toughness with time.

5. CONCLUSIONS

The micromechanisms of fracture and the toughness of a fibre composite can be displayed in the form of a map. These maps show how the fracture behaviour is affected by changes in the properties of the composite, give guidance in designing a composite for optimum toughness, and provide insight into the origins of environmental degradation. The application of these maps to predict the fracture stress of composite laminates containing holes and notches is important and needs to be pursued further.

6. REFERENCES

1. Wells, J.K. and Beaumont, P.W.R. "Debonding and pull-out processes in fibrous composites", paper in preparation.

2. Wells, J.K. and Beaumont, P.W.R. "Crack tip energy absorption processes in fibre composites", paper in preparation.

TABLE 1. MATERIAL PARAMETERS WHICH APPEAR IN THE MODELS

FIBRE	σ_f , E_f , r_f , m , ν_f
MATRIX	σ_m , E_m , G_l , ν_m
INTERFACE	μ , ε_o , ε_b , G_l
GEOMETRY	r_b , V_f

(f - fibre b - bundle m - matrix)

TABLE 2. TYPICAL VALUES OF MATERIAL PROPERTIES USED

	GLASS	KEVLAR	CARBON	
			HIGH MOD.	HIGH STRENGTH
E_1 (GPa)	35	76	220	140
E_2 (GPa)	5	5.5	9.8	9.8
G_{12} (GPa)	1.9	2.1	5.3	5.3
ν_{12}	0.3	0.34	0.34	0.34
σ_1 (GPa)	0.80	1.34	0.89	1.24
σ_2 (GPa)	55	29.6	60	66
τ_{12} (MPa)	85	60	83	83

	Fibre Radius r_f (μm)	Bundle Misfit Strain ϵ_b (%)
E-glass	7	5
Kevlar 49	6	4.3
Carbon	4	2.9

Fibre Type	G_1 (J m^{-2})
Carbon — High Modulus	24
Carbon — High Strength	61
Kevlar 49	2
E-glass	50

[Figures in brackets are not contoured on the maps]

FIBRE TYPE	$\bar{\ell}_{pf}$ (mm)	$\bar{\ell}_{pb}$ (mm)	ℓ_{db} (mm)	G (kJ m^{-2})	DOMINANT MECHANISM
GLASS	0.21	(∿ 0.1)	3.8	61	INTERFACE
KEVLAR	0.71	(∿ 0.3)	7.2	240	PULL-OUT
HIGH MODULUS CARBON	(0)	0.09	2.9	19	INTERFACE
HIGH STRENGTH CARBON	(0)	0.22	7.7	67	INTERFACE

TABLE 3. SUMMARY OF FRACTURE PROPERTY DEPENDENCE ON CONSTITUTIVE PROPERTIES OF THE COMPOSITE

COMPOSITE PARAMETER INCREASING	GLASS AND KEVLAR FIBRE COMPOSITES				CARBON FIBRE COMPOSITES			
	EFFECT ON			NOTE	EFFECT ON			
	ℓ_{pf}	ℓ_{db}	G		ℓ_{pb}	ℓ_{db}	G	
σ_f	↑	↑	↑	Direct effect on ℓ_p and ℓ_d	↑	↑	↑	
E_f	↓	↓	↓	Increases debond stress	↓	↓	↓	
σ_m	-	-	-	Negligible effect on strength of bundle	-	-	-	
E_m	↓	↓	↓	Residual stress for a given misfit strain affected	↓	↓	↓	
τ_f	↑	-	↑	Fibre debond stress and friction build-up affected	-	-	-	
τ_b	-	↑	↑	Reduced bundle debond stress and friction build-up	↑	↑	↑	
ϵ_o	↓	-	↓	Faster friction stress build-up	-	-	-	
ϵ_b	-	↓	↓	Faster friction stress build-up	↓	↓	↓	
G_1	↓	↓	↓	Debond stress and Interface energy	↓	↓	↓	
G_2	-	↓	↓	Debond stress and Interface energy	↓	↓	↑	
V_f	-	↑	↑	Increased number of fibres, increased bundle strength	↑	↑	↑	

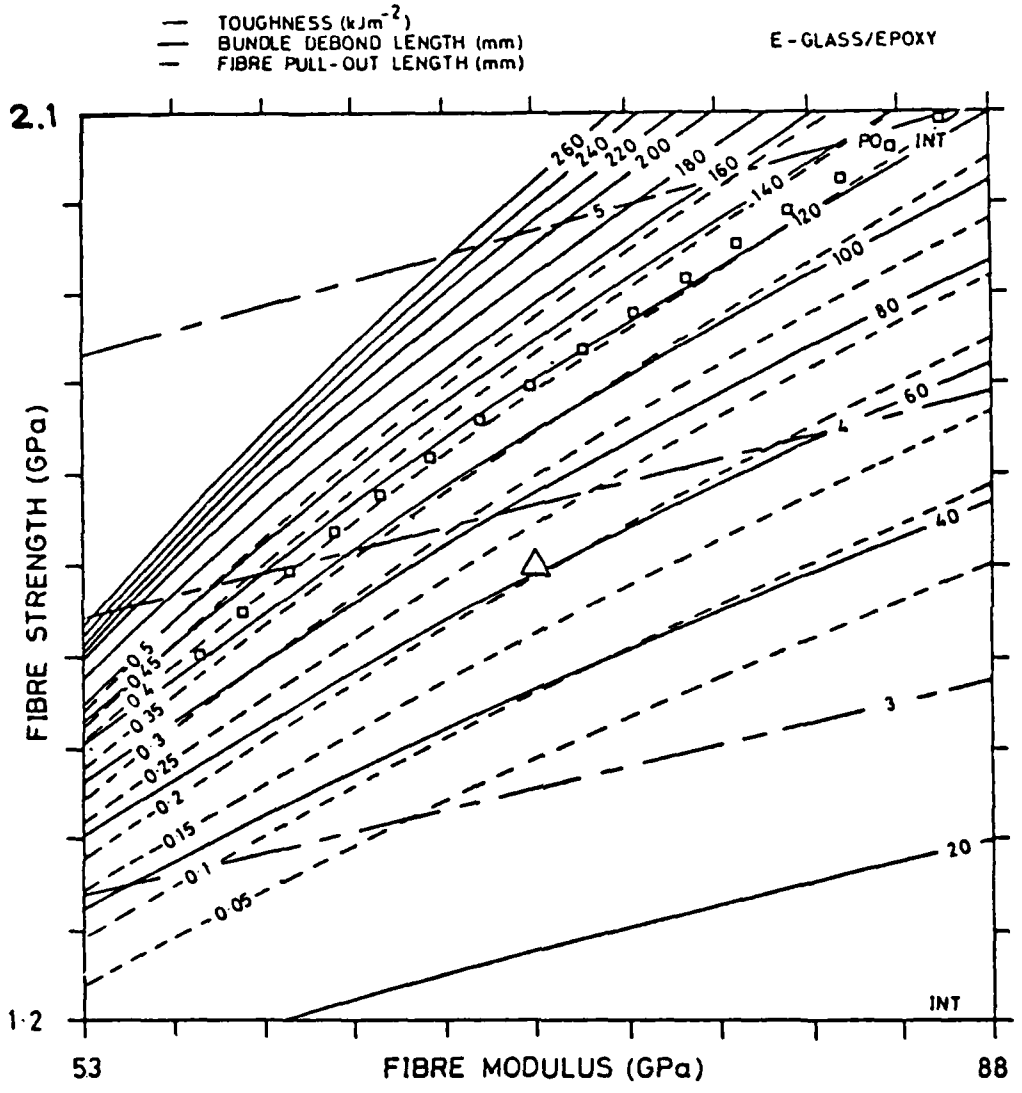

Fig. 1. A fracture map for E-glass/epoxy.

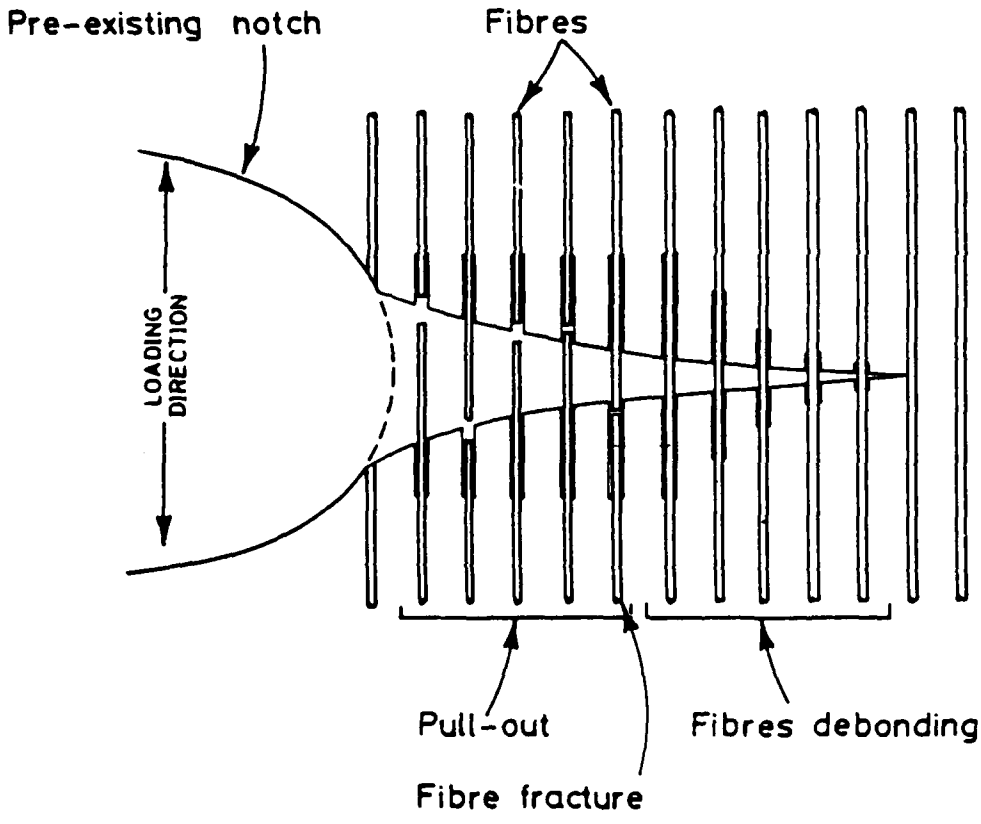

Fig. 2. A schematic of the crack tip region in a brittle, unidirectional fibrous composite.

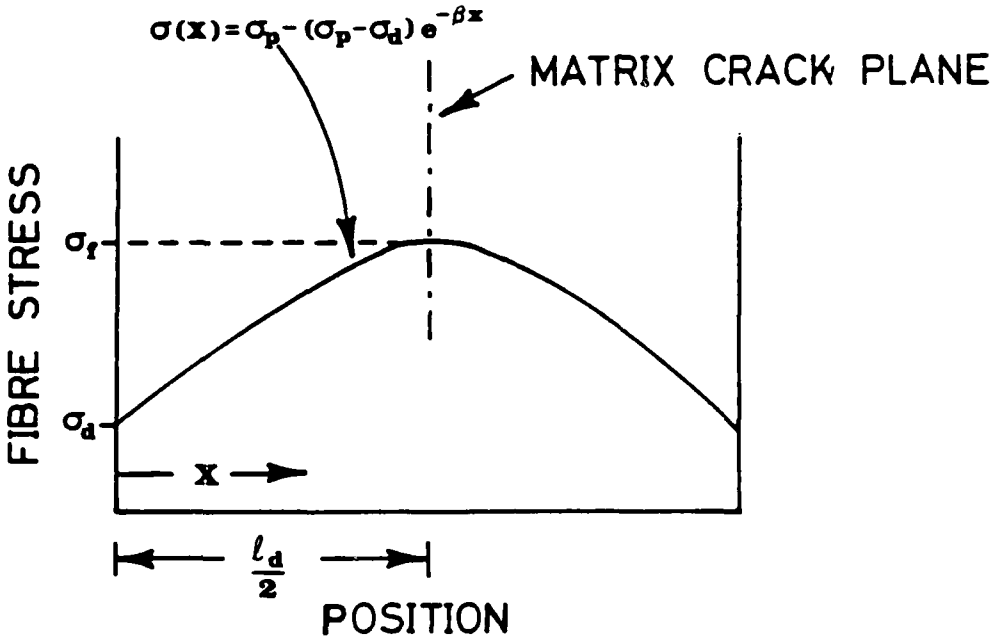

Fig. 3. Stress distribution along the length of a debonded fibre.

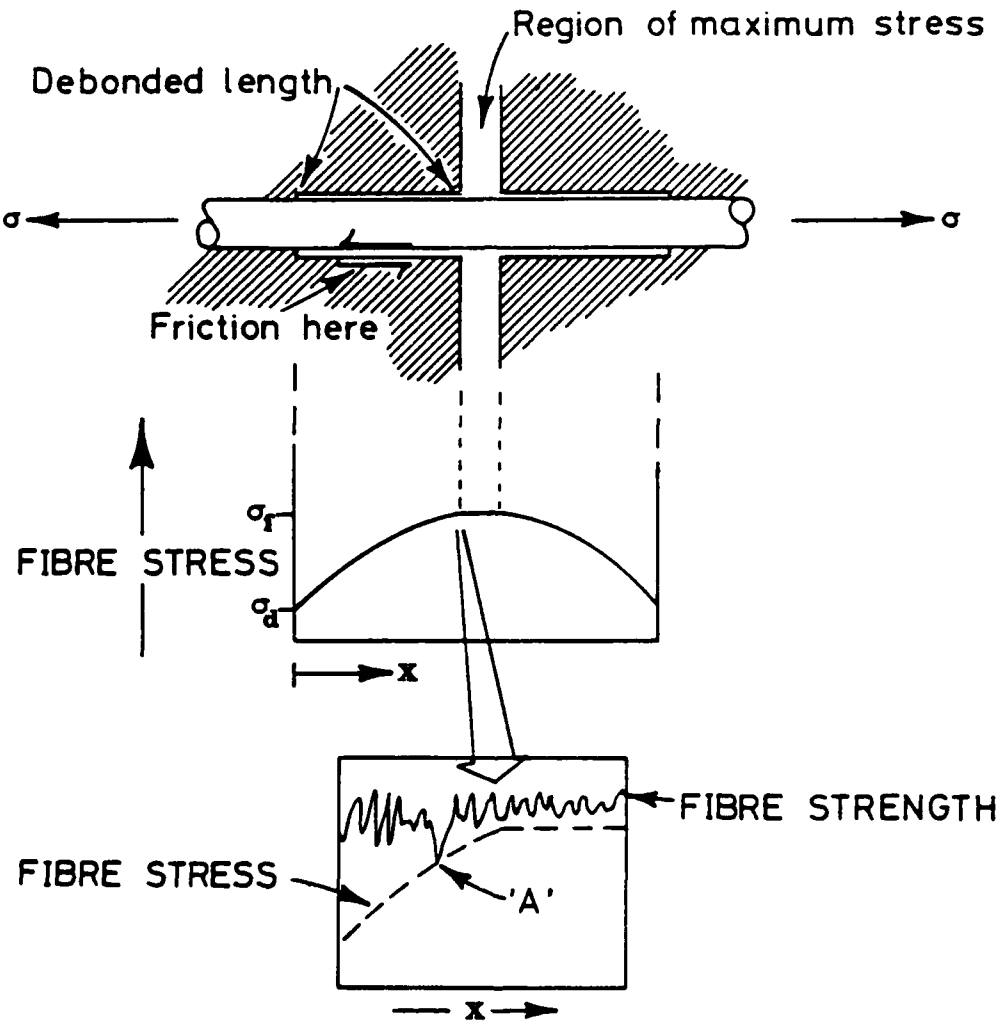

Fig. 4. Stress profile in a debonded fibre, together with the variation of fibre strength to show the location of a fibre break (point A).

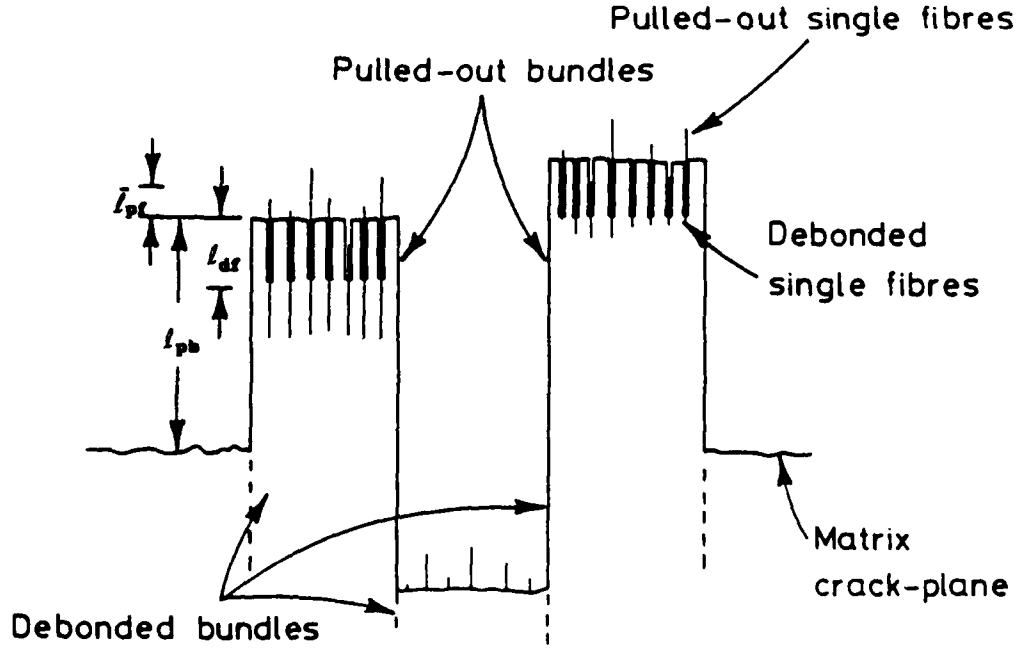

Fig. 5. Schematic of debonded and pulled-out fibres and bundles from a cracked matrix.

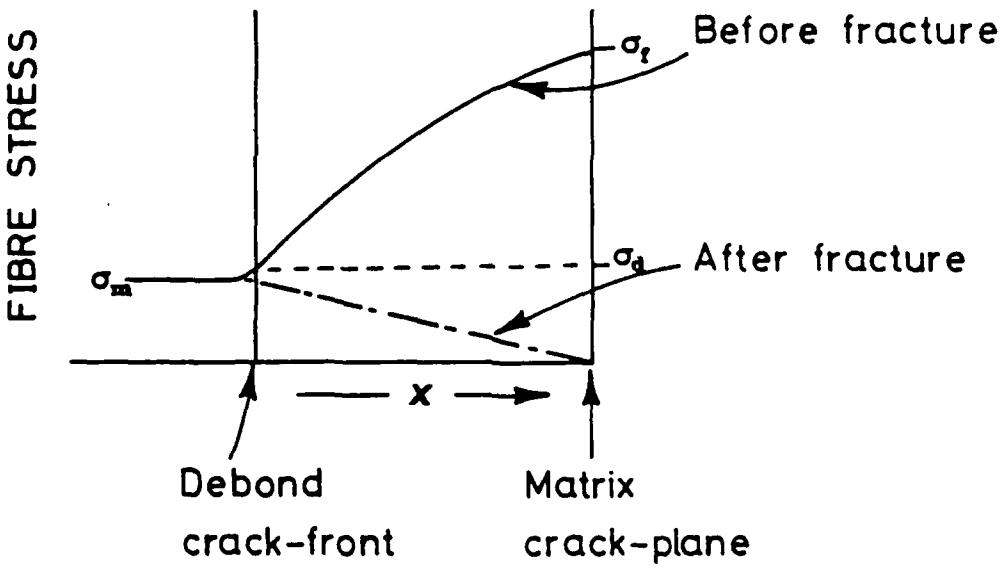

Fig. 6. Stress profiles in an unbroken and broken fibre.

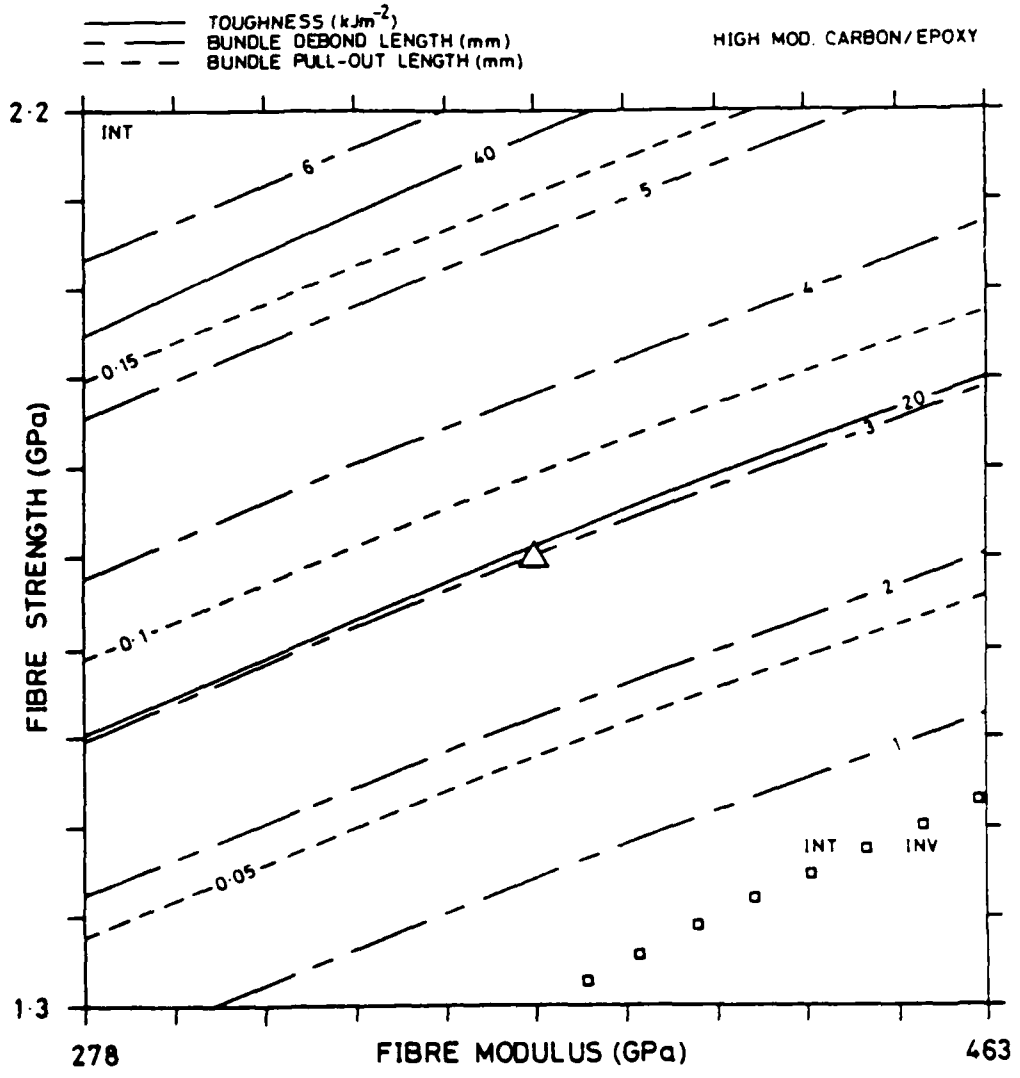

Fig. 7. A fracture map for HM carbon/epoxy.

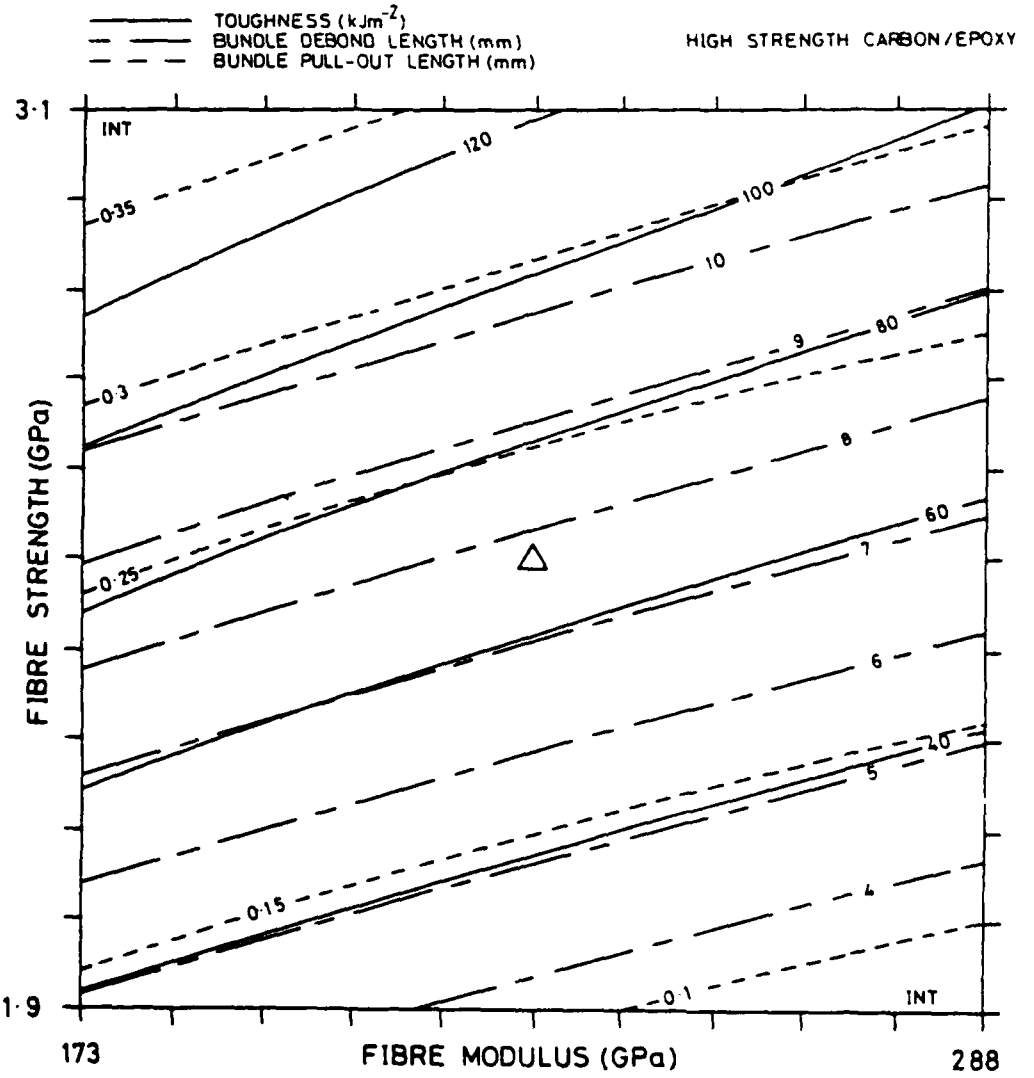

Fig. 8. A fracture map for HS carbon/epoxy.

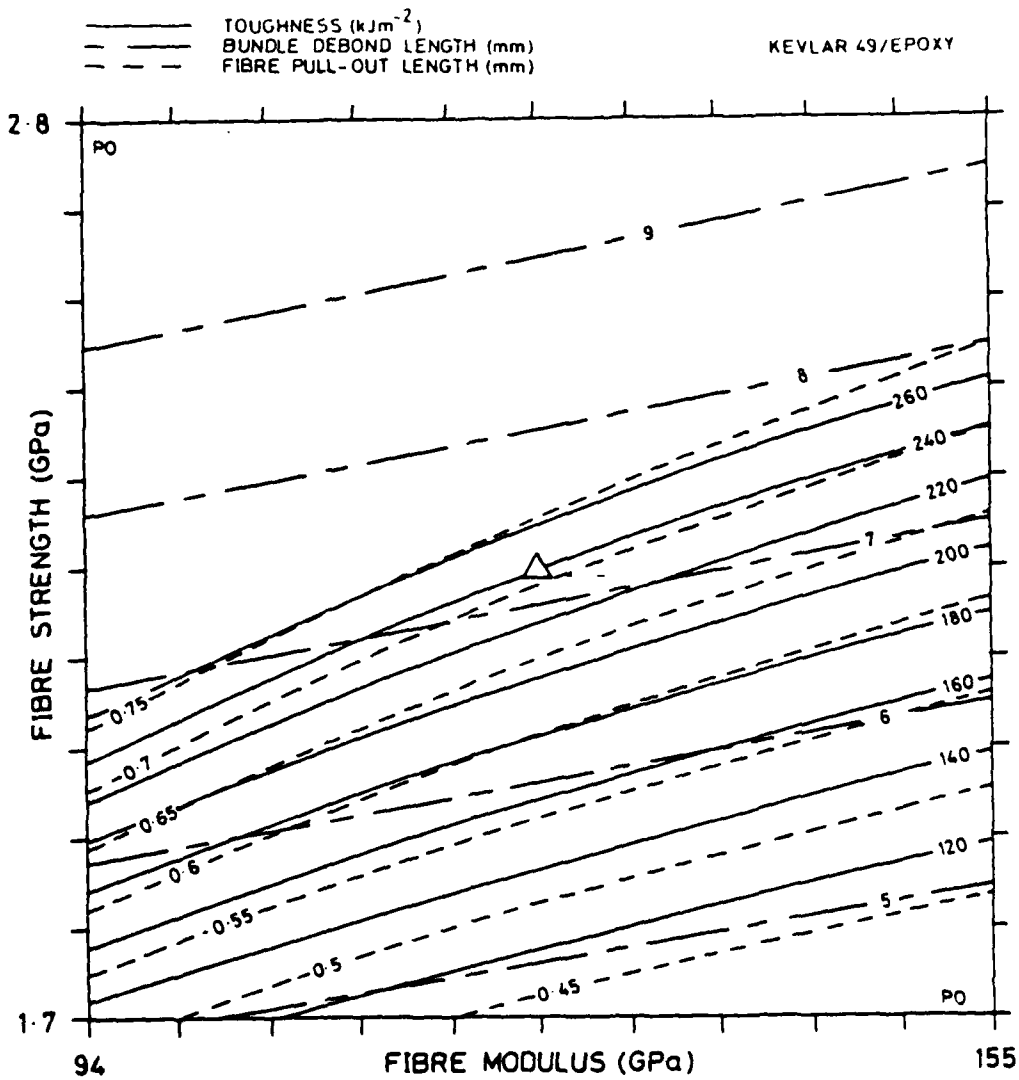

Fig. 9. A fracture map for Kevlar 49/epoxy.

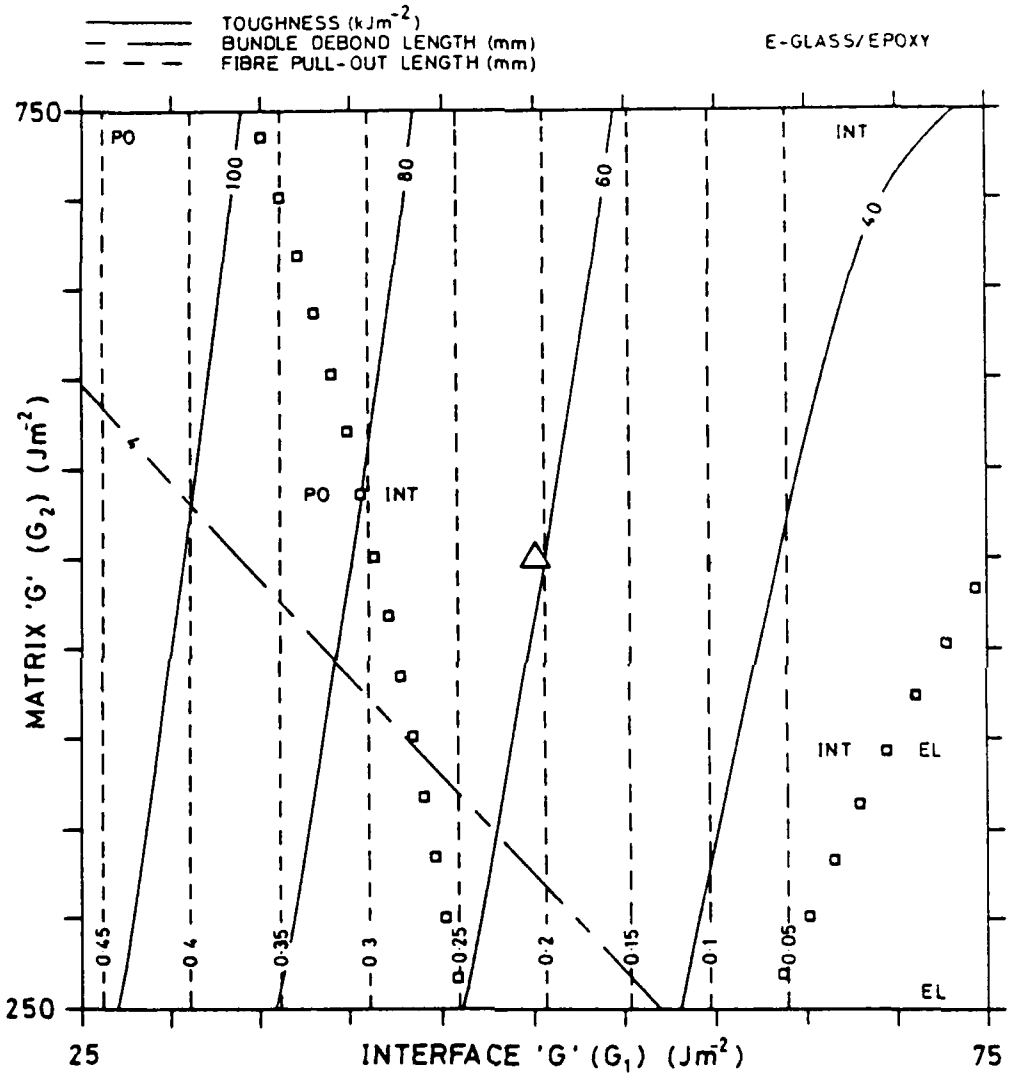

Fig. 10. A fracture map for E-glass/epoxy.

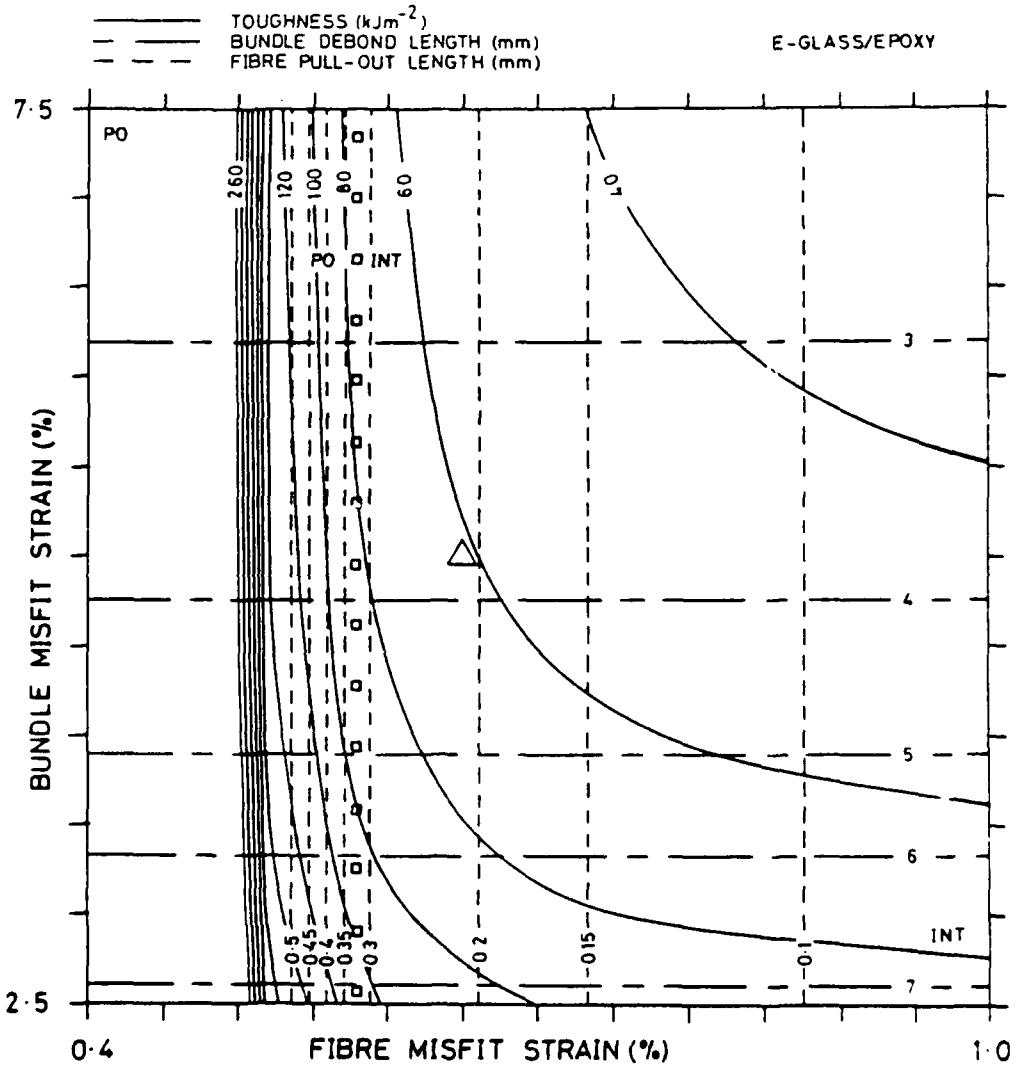

Figure 10. Cont'd.

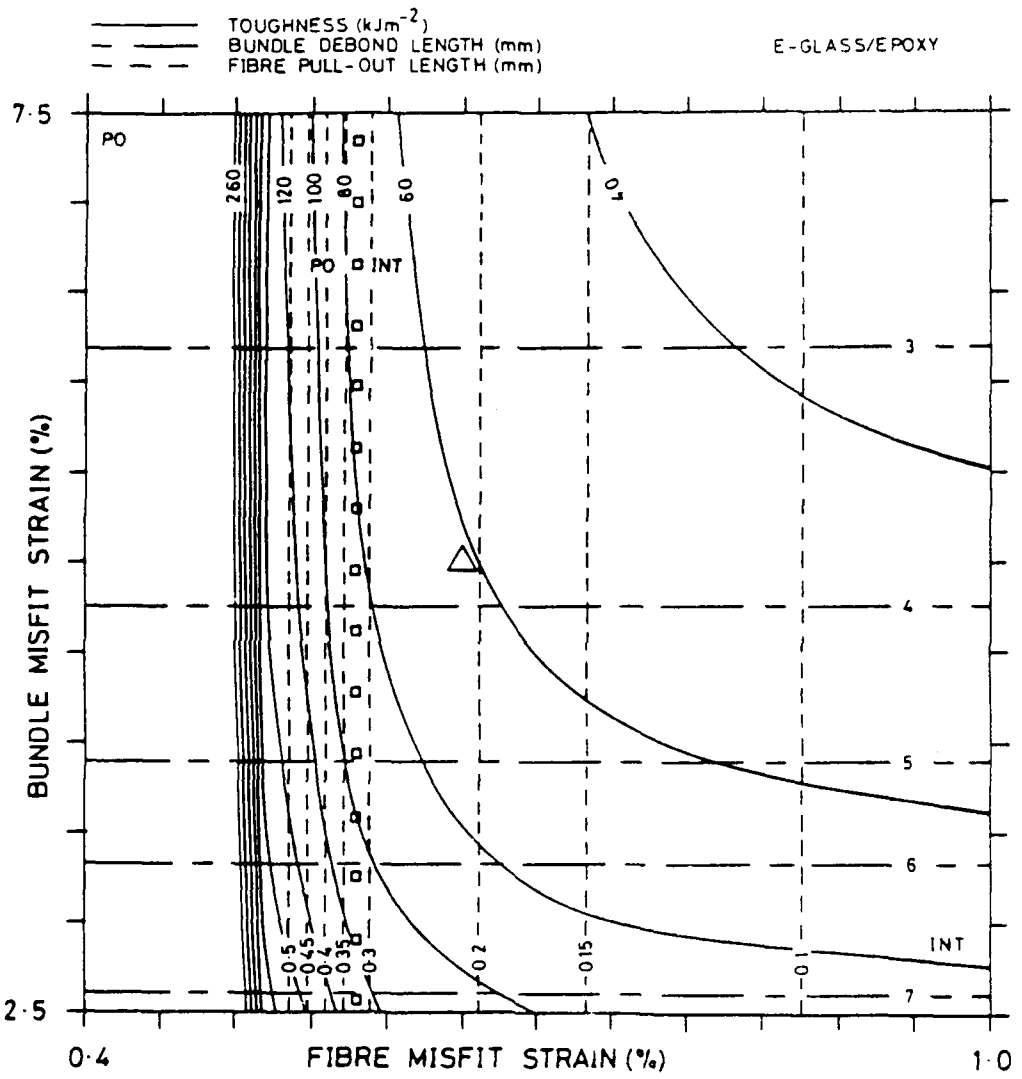

Figure 10. Cont'd.

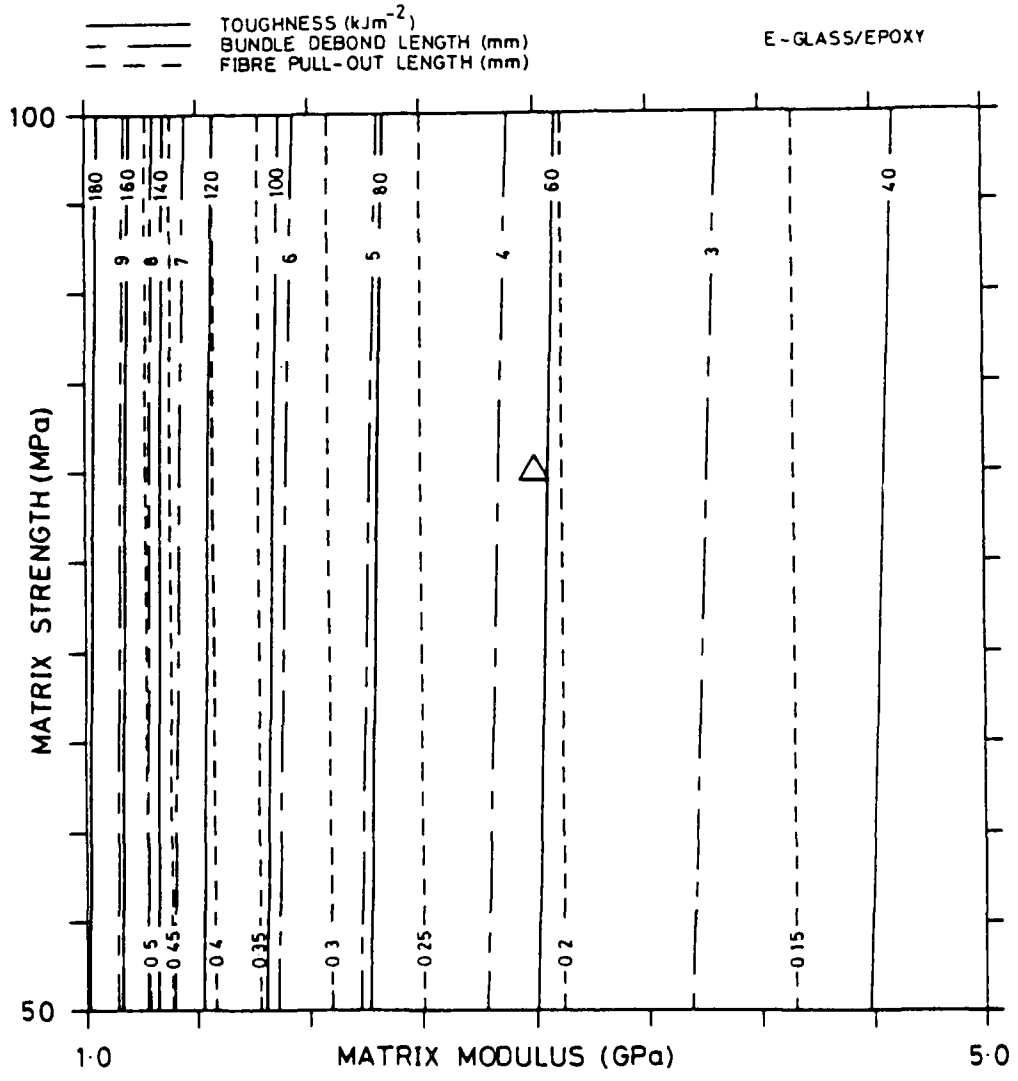

Figure 10. Cont'd.

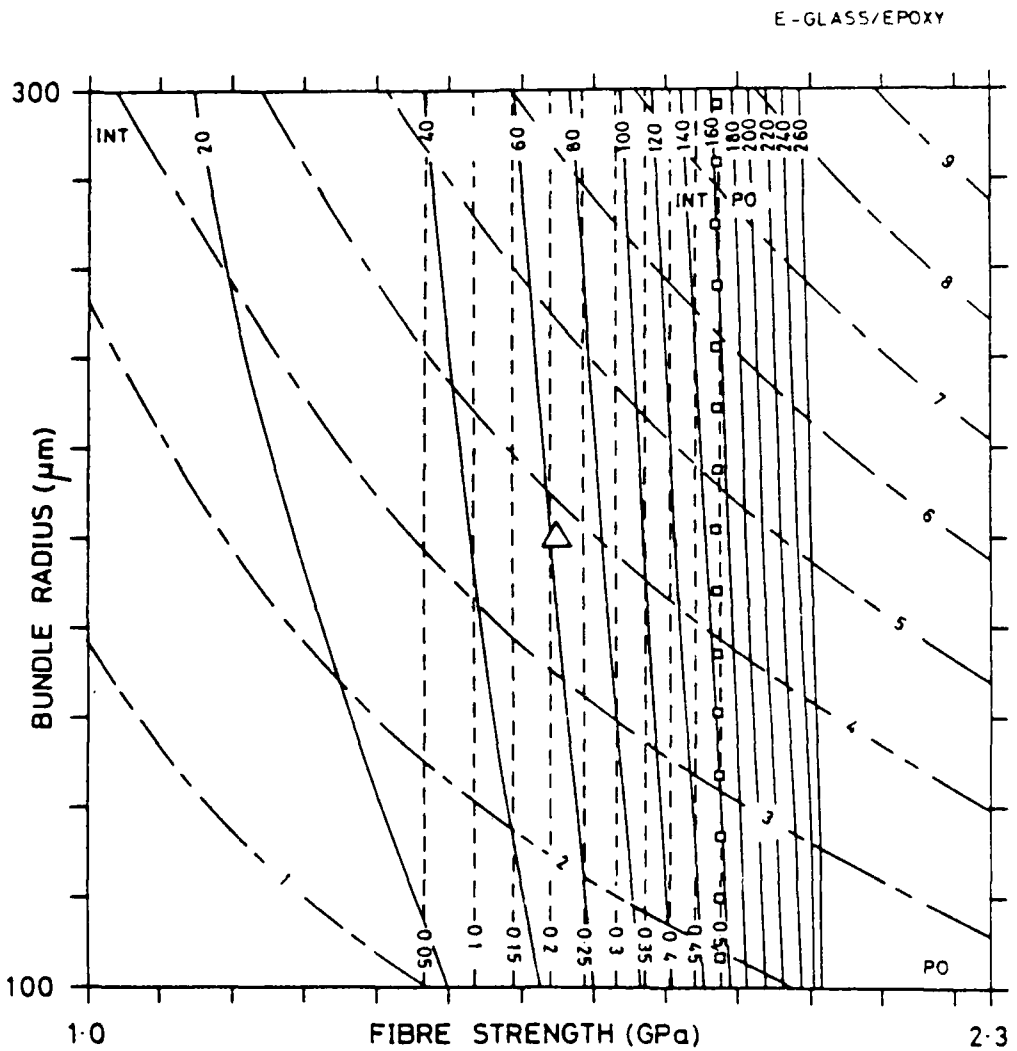

Figure 10. Cont'd.

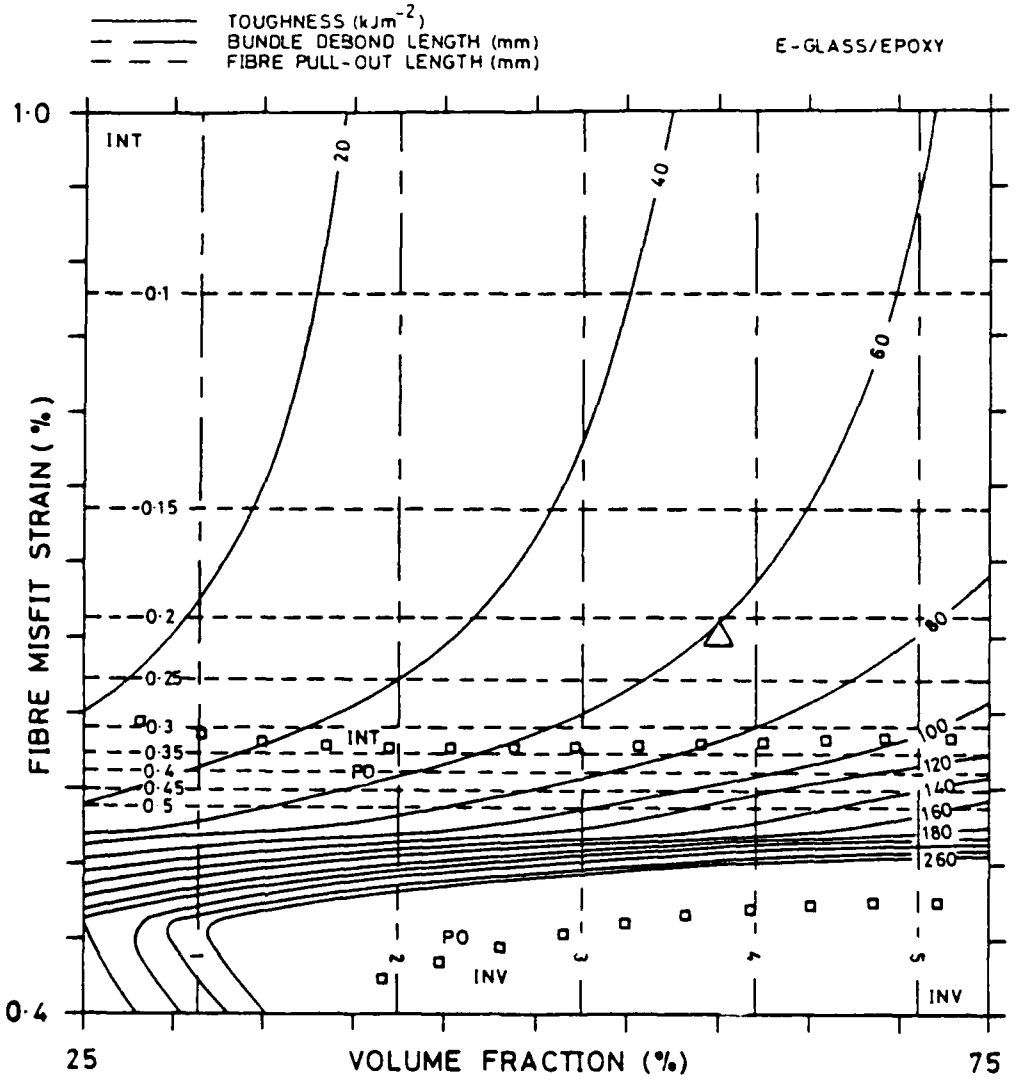

Figure 10. Cont'd.

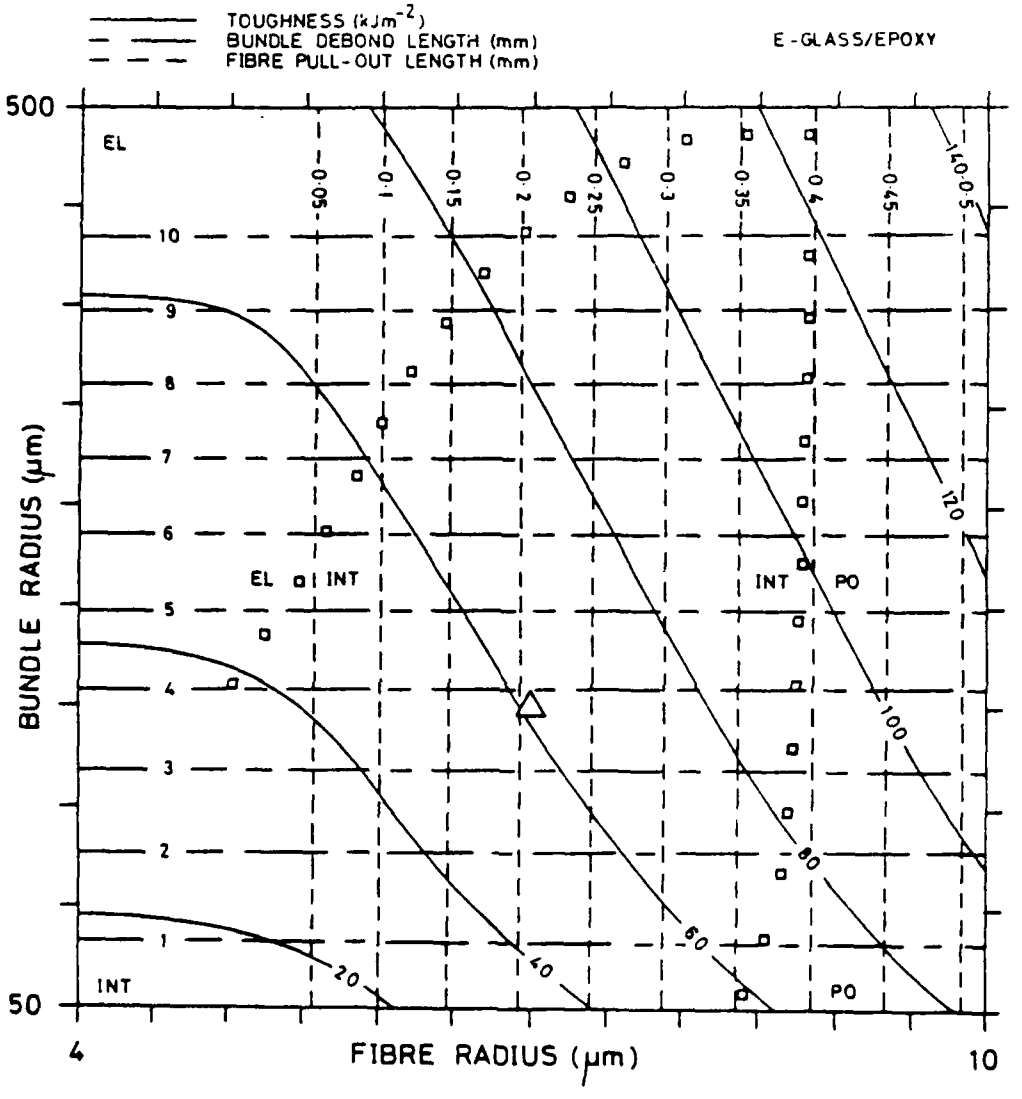

Figure 10. Cont'd.

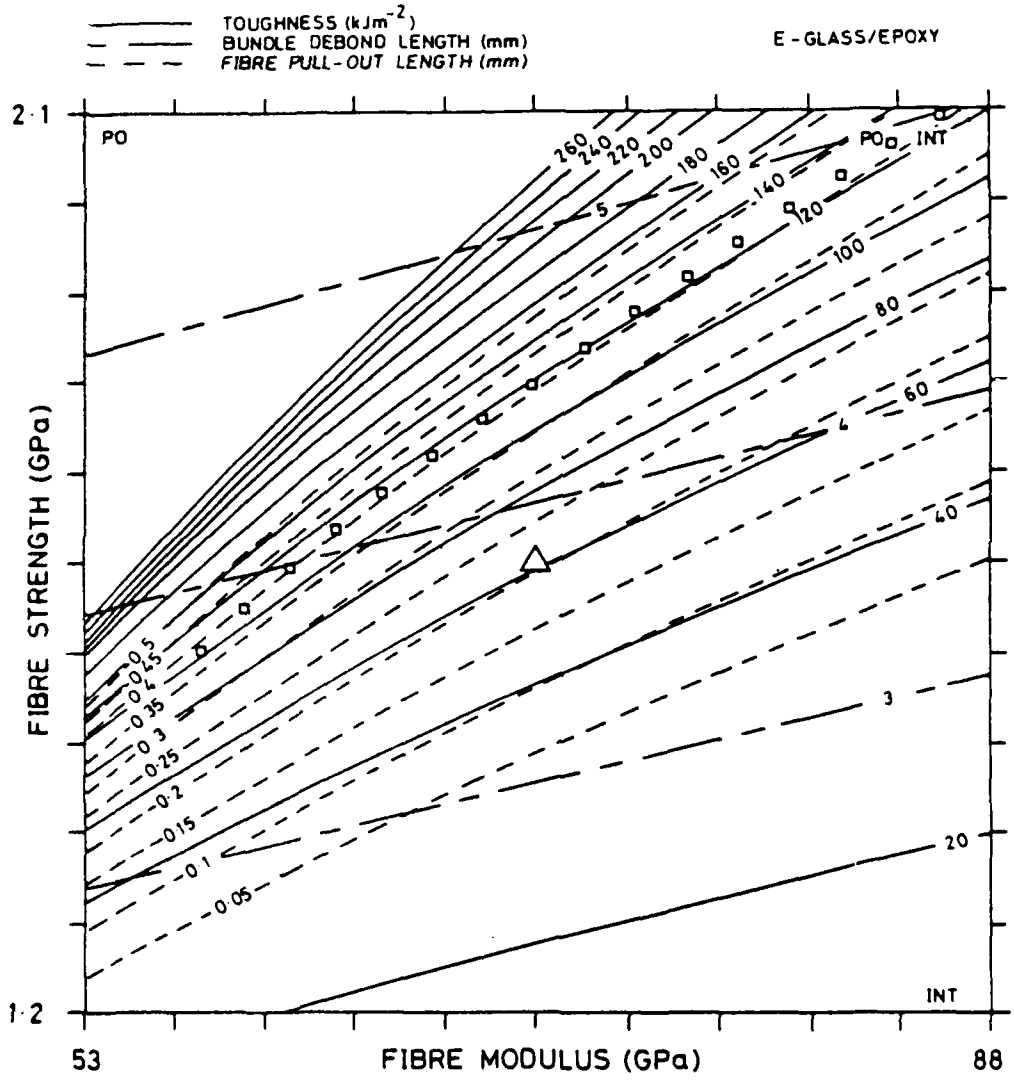

Figure 10. Cont'd.

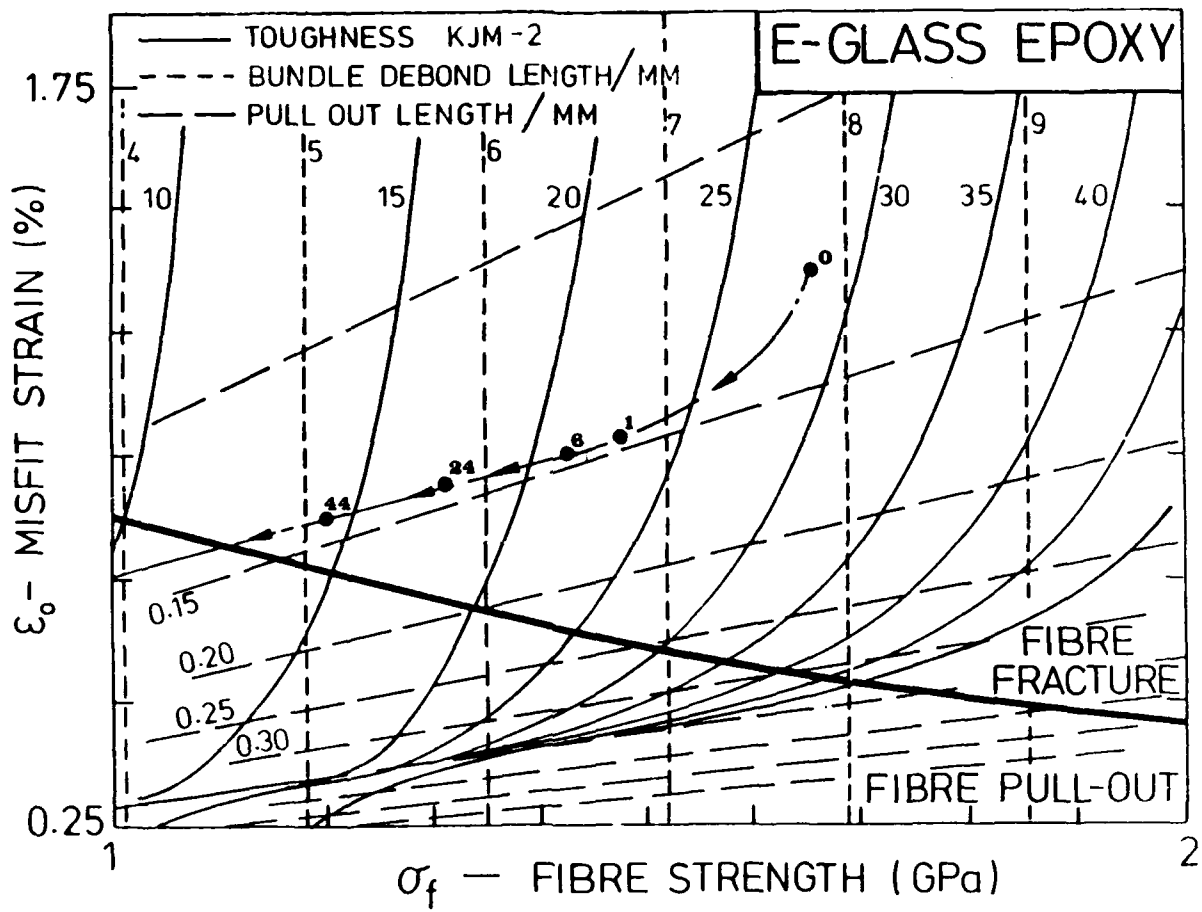

Fig. 11. A fracture map for (0/90) E-glass/epoxy with experimental toughness data superimposed. The numbers alongside each datum point refer to hours of exposure to steam.

Ashby, M. F.
Deformation and fracture maps for polymer-foams, solid polymers and polymer-composites / M. F. Ashby, P. W. R. Beaumont. -- Champaign, Ill : Construction Engineering Research Laboratory, 1984.
87 p (Technical manuscript ; M-344)

1. Polymers and polymerization--fracture. I. Beaumont, P. W. R. II. Title. III. Series : Technical manuscript (Construction Engineering Research Laboratory) ; M-344.